Lesson 14:

Special nanostructural changes
(Shape control of metal nanostructures embedded in insulating matrices by high energy ion irradiations: elongation and inverse ripening; Thermodynamic instability of nanorods and spontaneous reshaping; Shadowed depositions of films on substrates to produce complex-morphology nanostructures; Nanoparticles embedding in polymeric films)

# Reshaping of nanorods (by thermal instability)

Below Melting Point Photothermal Reshaping of Single Gold Nanorods Driven by Surface Diffusion

Adam B. Taylor, Arif M. Siddiquee, and James W. M. Chon*

Centre for Micro-Photonics, Faculty of Science, Engineering and Technology, Swinburne University of Technology, P.O. Box 218, Hawthorn 3122, Victoria, Australia

ABSTRACT Plasmonic gold nanorod instability and reshaping behavior below melting points are important for many future applications but are yet to be fully understood, with existing nanoparticle melting theories unable to explain the observations. Here, we have systematically studied the photothermal reshaping behavior of gold nanorods irradiated with femtosecond laser pulses to report that the instability is driven by curvature-induced surface diffusion rather than a threshold melting process, and that the stability dramatically decreases with increasing aspect ratio. We successfully utilized the surface diffusion model to explain the observations and found that the activation energy for surface diffusion was dependent on the aspect ratio of the rods, from 0.6 eV for aspect ratio of 5 to 1.5 eV for aspect ratio less than 3. This result indicates that the surface atoms are much easier to diffuse around in larger aspect ratio rods than in shorter rods and can induce reshaping at any given temperature. Current plasmonics and nanorod applications with the sharp geometric features used for greater field enhancement will therefore need to consider surface diffusion driven shape change even at low temperatures.
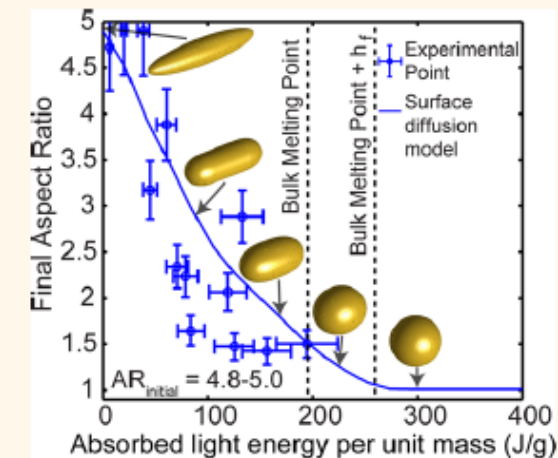
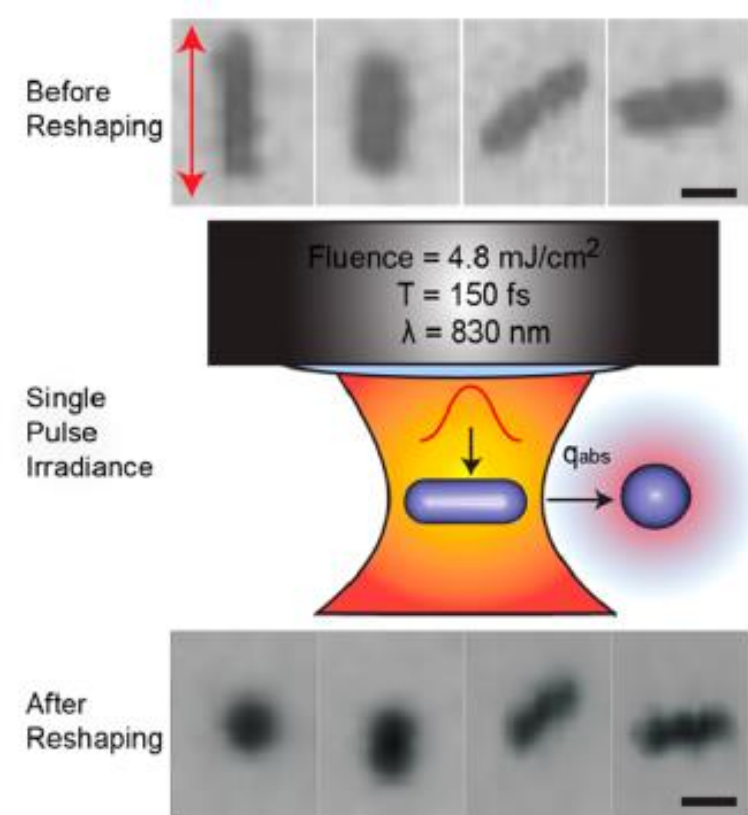**KEYWORDS:** gold nanorods · photothermal reshaping · surface diffusion · plasmonics

Figure 1. (a) Schematic showing the angular depletion method of photothermal reshaping: Nanorods are imaged on a coordinate-marked TEM slide in a precise location, then a single pulse is applied to all the nanorods to heat and reshape them, and finally, the same rods are located and imaged again to quantify the degree of reshaping. TEM image of the same nanorods before and after single pulse excitation with vertically polarized light. Scale bar is 20 nm. Note that as the orientation
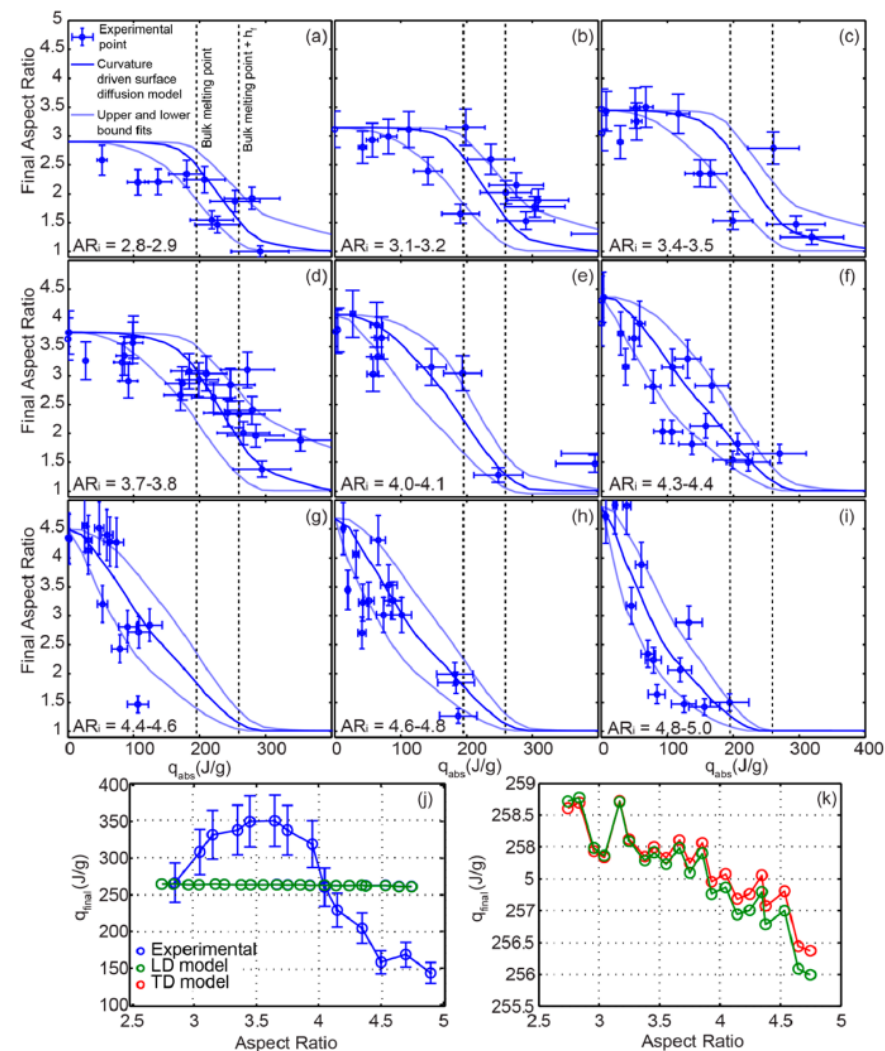

Figure 2. (a−i) Photothermal reshaping behavior of gold nanorods in respective aspect ratio range bins. Final aspect ratio vs absorbed energy density q_{abs}. Aspect ratio ranges from 2.7 to 5.0. Points with error bars are experimental results. Solid blue lines are the theoretical simulation using eqs 1−4; see text. The two vertical lines indicate the energy density needed to reach the melting temperature and to overcome the latent heat of fusion h_f. (j) Complete reshaping point q_{final} vs the aspect ratio extracted from the panels a−i. Black and red lines are the existing theoretical complete reshaping points, $i.e.$, q_{final}^{theory}. Thermodynamic model[24] and liquid-drop model[28,32] calculated for average aspect ratio and volume of the nanorods within each bin. (k) Close-up view of theory lines of q_{final}^{theory} values showing only a small change around 255 J/g.

Previously, Mullins[37-39] proposed a theory on the curvature driven reshaping and successfully explained the blunting of field emission gun tips in electron microscope or scanning tunneling microscope tips below the melting point. The central idea of this theory is the surface diffusion acting to minimize the surface energy of an object. The surface flux of diffusing atoms $\mathbf{J}_s$ can be expressed by

$$\mathbf{J}_s = \frac{\Omega v_s}{kT} \vec{\mathbf{D}}_s \cdot \nabla \mu \tag{1}$$

where Ω is an atomic volume, v_s is the number of diffusing surface atoms in the unit area, k is the Boltzman's constant, T is temperature, and μ is the chemical potential. $\vec{\mathbf{D}}_s$ is the interface diffusivity tensor. The gradient notation ∇ is two-dimensional on the surface. Equation 1 should satisfy the equation of continuity, $(\partial n/\partial t) + \nabla \cdot \mathbf{J}_s = 0$, where $\partial n/\partial t$ represents the movement speed of a point on the surface in the outward normal direction to the surface. For an isotropic surface, the diffusivity tensor can be simplified as $D_s(T)$, with typical Arrhenius behavior with an activation energy E_a and a constant D_0 as

$$D_s(T) = D_0 \exp\left(\frac{-E_a}{kT}\right) \tag{2}$$

The chemical potential μ can also be simplified for an isotropic surface, following the Herring's formula[37,40]

$$\mu = \mu_0 + \gamma_s \Omega K \tag{3}$$

where $K = 1/R_x + 1/R_y$ is the mean curvature of the surface, γ_s is the free energy, and μ_0 is the chemical potential for a flat surface. Equation 1 becomes

$$\frac{dn}{dt} = v = B\nabla^2 K \tag{4}$$

where $B = (\Omega^{4/3}\gamma_s D_s)/(kT)$. The equation relates the movement speed of a surface point to the curvature driven surface diffusion.
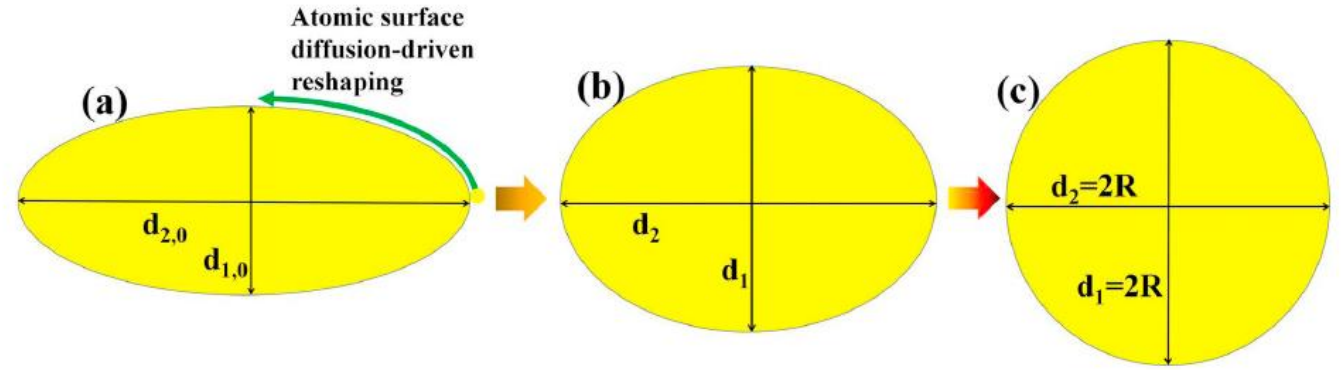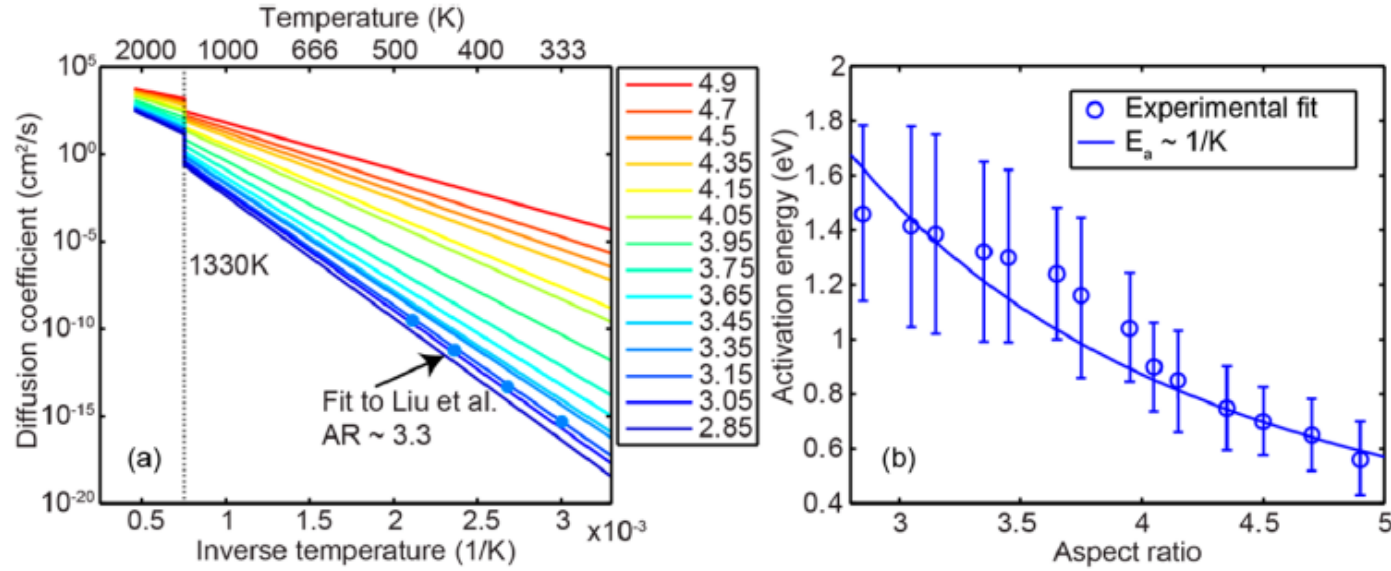

Fig. 5. Representative scheme of the single isolated NR reshaping process (towards the spherical shape) based on Au atomic surface diffusion-driven phenomenon.
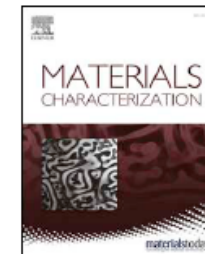
Figure 4. (a) Temperature-dependent surface diffusion coefficients $D_s(T)$ used for the theoretical fitting with eq 3 to the experimental data for a range of initial aspect ratios. The points indicate the diffusion coefficients used to fit Liu et al.'s experimental results.[17] (b) Activation energies used for the best fit to the experimental points in Figure 2. Overlaid is the ~1/K activation energy relation with respect to aspect ratio, where K is the tip curvature.

Independent of the surface diffusion model, predicting the activation energy trend for nanorods requires boundary conditions where E_a at AR ~ 1 (sphere) should be a finite value and E_a at AR $\sim \infty$ should converge to 0. A linear fit line fails to meet this condition, as it predicts a physically untenable negative value of E_a. Previously, the activation energy for the below melting point nucleation of crystal facets due to surface diffusion was predicted to follow $E_a \sim 1/K$.[42] In terms of the dimensions of the rods, the $E_a \sim 1/K$ curve has the following expression

$$E_a = \frac{2aC}{(AR^2 + 1)} \tag{5}$$

where a is the one-half nanorod length and C is a constant of proportionality (refer to Supporting Information 5 for the derivation). Applying a similar argument, the $E_a \sim 1/K$ curve for ellipsoidal nanorods is overlaid on Figure 4b. The trend is in a reasonable agreement with the experimental results, with an extracted value of C from Figure 4b of $C = 2.6 \times 10^8$ eV/m. It is noted that the curvature K is dependent on the aspect ratio and the dimensions of the rod (a in this case). Therefore, the aspect ratio dependencies of both curvature K and activation energy E_a have to be understood within the specified size regime.

Shape design of supported Au nanorods through morphological evolution: Coalescence, instability, reshaping

M. Censabella, M.G. Grimaldi, F. Ruffino*

Dipartimento di Fisica e Astronomia Università di Catania and MATIS CNR-IMM, via S. Sofia 64, 95123 Catania, Italy

ARTICLE INFO

ABSTRACT

The morphological evolution of surface supported Au nanorods, induced by thermal heating, has been examined. This study is focused on the establishment of the connection of the nanorods morphology to the annealing temperature, on the elucidation of the acting microscopic mechanisms and quantitative evaluation of the involved parameters leading to the morphology evolution.

In particular, after depositing the nanorods on SiO_2 surface, thermal processes were performed to induce their morphological evolution and we pointed out our attention on:
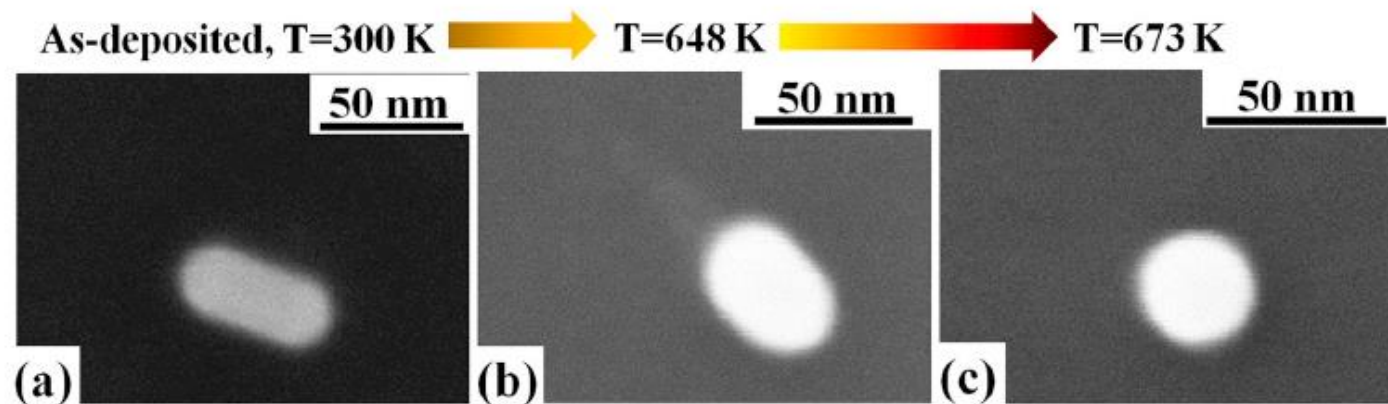
a) the study of the morphological evolution of single isolated Au nanorods, which was identified as a reshaping process towards a spherical shape. The morphological analysis led us to establish the correlation between the annealing temperature and the nanorods aspect ratio and to elucidate the basic atomic driving mechanism for the reshaping process;

b) the study of the morphological evolution of closely spaced nanorods (forming a film over the substrate surface). The analysis led us to the identification of the mechanisms governing the nanorods joining and evolution in larger architectures which, then, operate a reshaping process.

On the basis of the results, we set a general framework for the design of complex morphology nanostructures on surfaces with desired shape and aspect ratio.
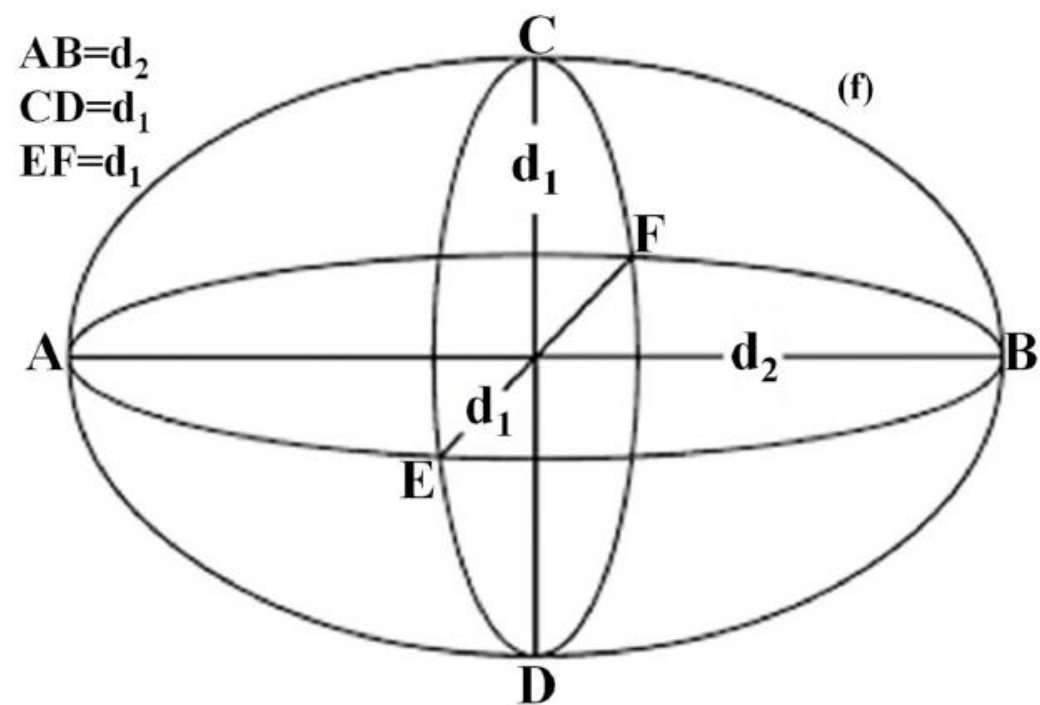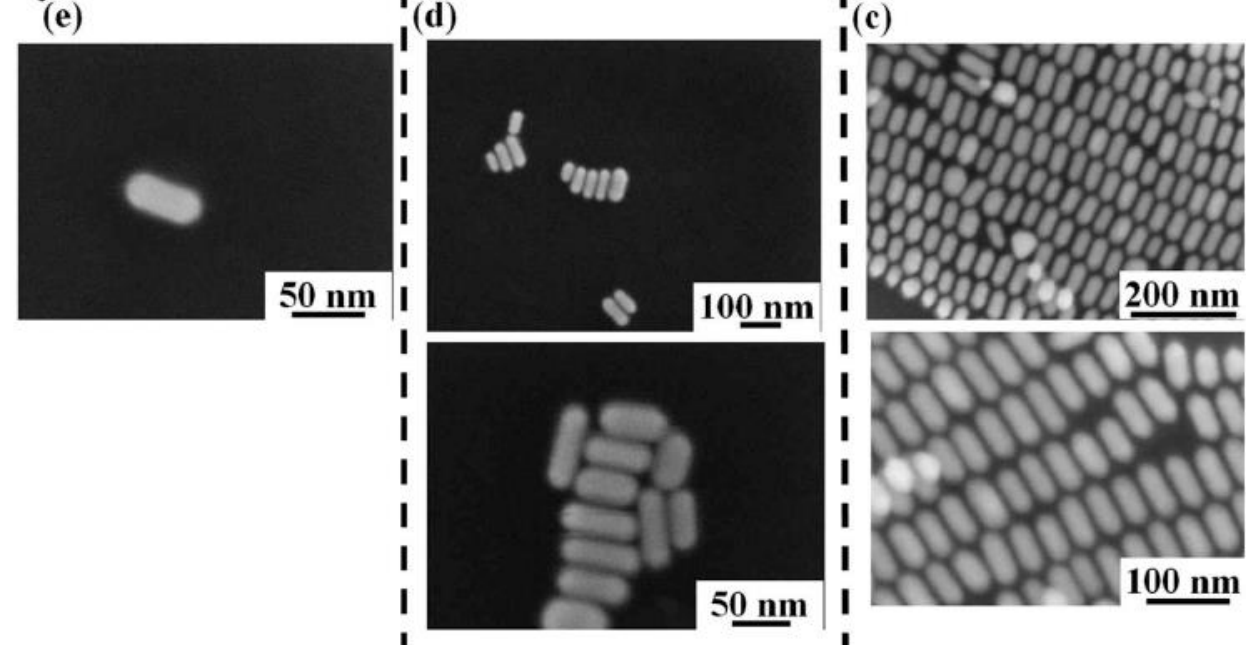
the SEM image in (e). (f) Modeling of the starting shape of the as-deposited NRs: each NR is represented by an ellipsoid with two equal sizes d_1 ($=d_{1,0} \approx 25$ nm) and a third larger size d_2 ($=d_{2,0} \approx 60$ nm).

$AB=d_2$
$CD=d_1$
$EF=d_1$

Fig. 2. Sequence of SEM images to represent the morphological evolution of a single isolated NR (in region 1) as a function of the annealing temperature: starting from the as-deposited Au NR ((a)) with $d_1 = d_{1,0} \approx 25$ nm and $d_2 = d_{2,0} \approx 60$ nm ($AR = AR_0 = 2.4$) the annealing processes for $T < 673$ K (648 K as in the example in (b)) causes the increase of d_1 and decrease of d_2 (decrease of AR) till to $T \geq 673$ K ((c)) for which the reshaping process is complete and the starting NR acquired a spherical shape ($AR \approx 1$).
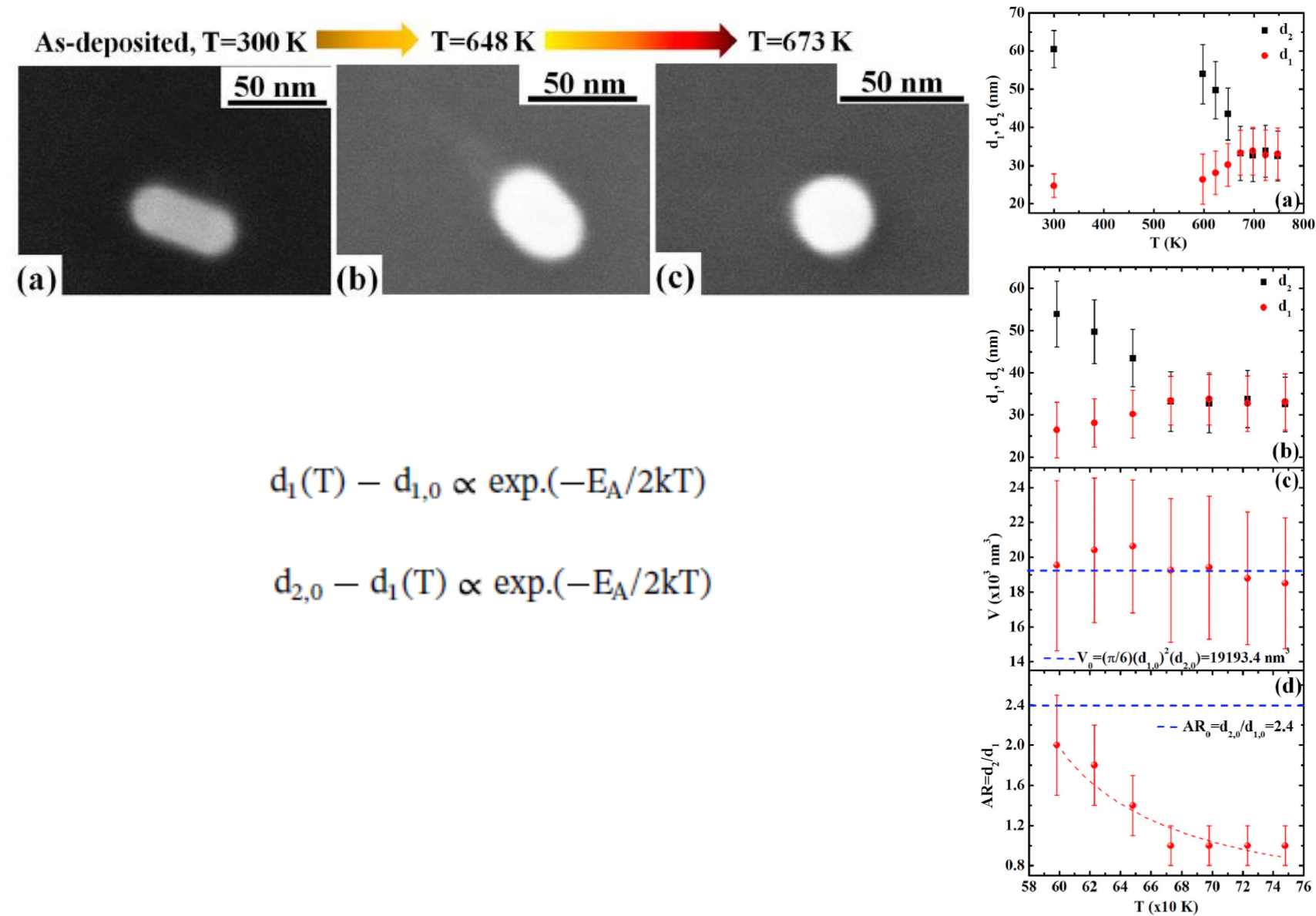
As-deposited, T=300 K → T=648 K → T=673 K

As-deposited, T=300 K → T=648 K → T=673 K

(a) 50 nm (b) 50 nm (c) 50 nm

$$d_1(T) - d_{1,0} \propto \exp.(-E_A/2kT)$$

$$d_{2,0} - d_1(T) \propto \exp.(-E_A/2kT)$$

Fig. 3. (a) and (b): plots of d_1 and d_2 (mean values) as a function of annealing temperature T. (b) is (a) restricted from 598 K to 748 K to evidence the increase of d_1 and the corresponding decrease of d_2 when T increases from 598 K to 673 K and that $d_1 \approx d_2 \approx$ constant for 673 K $\leq T \leq$ 748 K. Using, for each T, the evaluated mean values for d_1 and d_2, (c) reports the calculated volume for the NRs compared to the volume V_0 of the starting as-deposited single NR. (d) Reports the evolution of the aspect ratio AR (evaluated as the ratio of the mean values d_2/d_1) for the NRs as a function of the annealing temperature T: AR decreases from, about, 2.4 to, about, 1 (when the NRs became nanospheres) when T increases from 598 K to 673 K and then, further increasing T, it is constant to, about, 1.
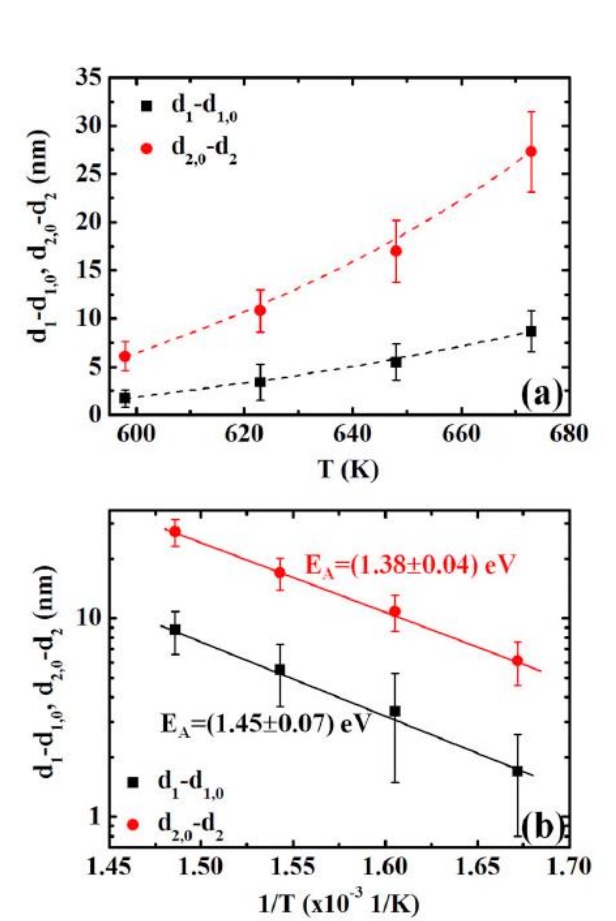
Fig. 4. (a) Plot of the differences $d_1 - d_{1,0}$ and $d_{2,0} - d_2$ versus T in linear scales (where $d_{1,0}$ and $d_{2,0}$ are the mean values of d_1 and d_2 for $T = 300$ K, i.e. for the as-deposited NRs, and d_1 and d_2 are the mean values for the annealing temperatures $T > 300$ K). (b) Plot of the differences $d_1 - d_{1,0}$ and $d_{2,0} - d_2$ versus 1/T with the vertical axis in Log scale. Dots are the experimental data and the full lines are exponential fits.

In the present case, the starting AR of the used NRs is $AR_0 = 2.4$. The model developed by Taylor et al. indicates that, corresponding to $AR_0 = 2.4$, the activation energy for the Au atomic surface diffusion should be, roughly, in the 1.40–1.70 eV range. So, the experimental evaluated $E_A \approx 1.42$ eV by us is in full agreement with this model. Basing on this result, we can conclude, hence, that the Au NRs reshaping process is the curvature driven Au atomic surface diffusion as schematized in Fig. 5 (the scheme, for sake of simplicity, reports a two-dimensional representation of the process while, obviously, the process should be thought as acting in three dimensions). The surface diffusion acts to minimize the surface energy of the NR, whereas the flux of surface diffusing atoms is proportional to the gradient of the chemical potential. In addition the chemical potential is inversely proportional to the mean curvature of the surface of the NR. Overall, the reshaping process involves the surface migration of atoms from the high curvature (i.e., tip) to the low curvature (i.e., waist) regions of the NR (see Fig. 5). It is worth to observe that the results obtained by Taylor et al. explain our results even if the experimental conditions under which the Au NRs reshaping process takes place are significantly different (femtosecond laser induced photo-thermal reshaping in the case of Taylor et al., standard equilibrium thermal processes performed by us). This fact could indicate the universal nature of the curvature driven Au atomic surface diffusion as driving process for the NRs reshaping. It is worth,
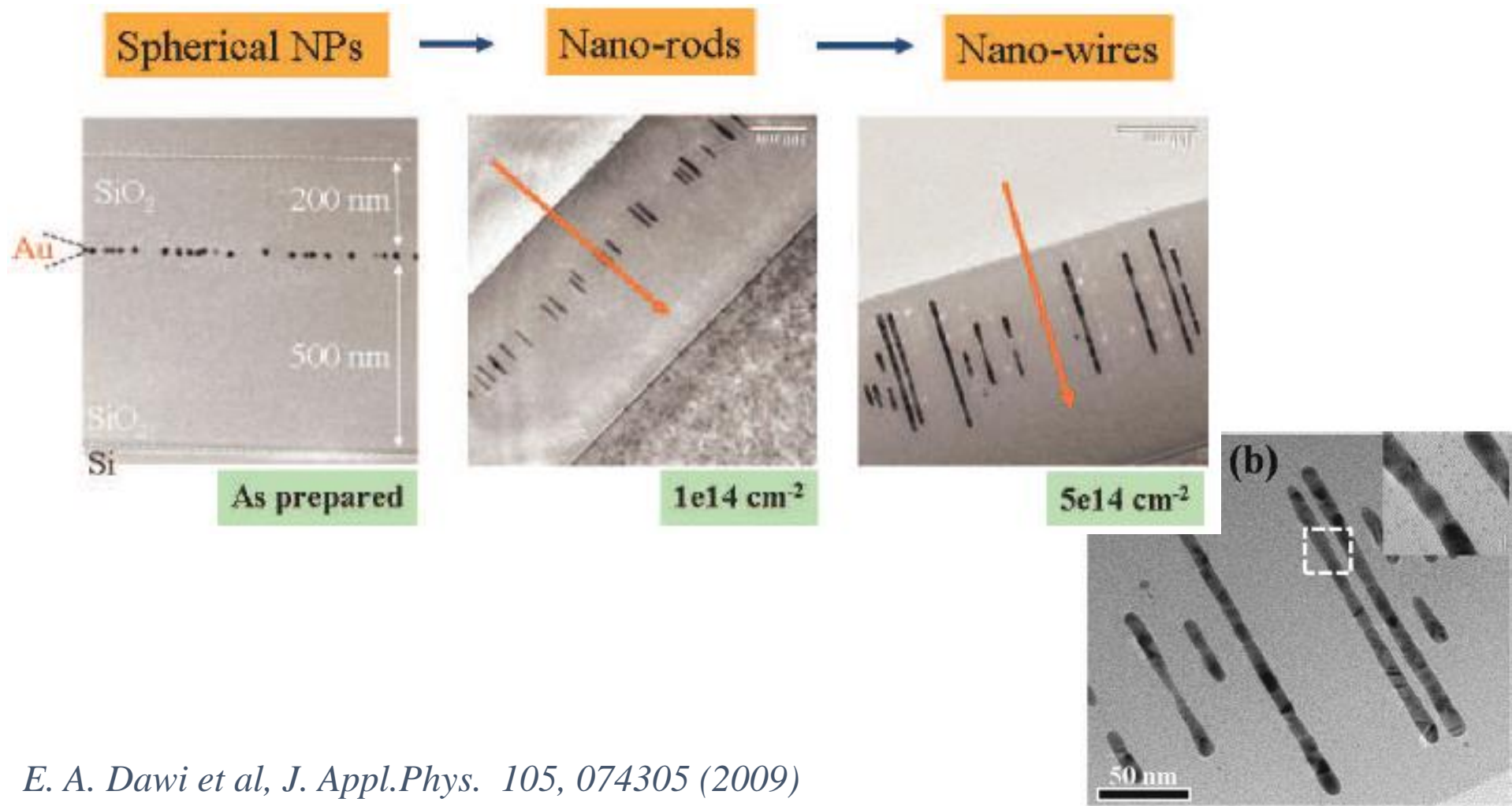

(a) Atomic surface diffusion-driven reshaping $d_{2,0}$ $d_{1,0}$ (b) d_2 d_1 (c) $d_2=2R$ $d_1=2R$
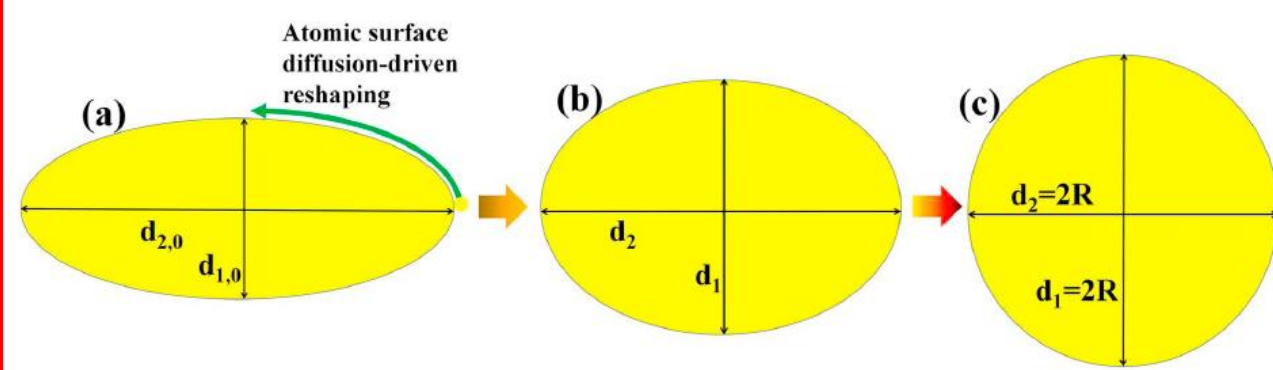
Ion beam shaping of metal nanostructures embedded in oxide matrices

Deformation can be indirectly induced by embedding metallic NPs into an ion-deformable amorphous host matrix. With this technique, **spherical particles deform into prolate nanorods and nanowires, with an aspect ratio that can be tuned by the ion type, energy and fluence**

Spherical NPs →	Nano-rods →	Nano-wires
As prepared	1e14 cm^{-2}	5e14 cm^{-2}

E. A. Dawi et al, J. Appl.Phys. 105, 074305 (2009)

Rational description of the ion-beam shaping mechanism

G. Rizza[*] and P. E. Coulon

Ecole Polytechnique, Laboratoire des Solides Irradiés, CEA-IRAMIS-CNRS, 91128 Palaiseau Cedex, France

V. Khomenkov, C. Dufour, I. Monnet, and M. Toulemonde

CIMAP-ENSICAEN-CEA-CNRS, University of Caen, Bd H. Becquerel, Boîte Postale 5133, 14070, Caen Cedex 5, France

S. Perruchas and T. Gacoin

Ecole Polytechnique, Laboratoire de Physique de la Matière Condensée, CNRS, 91128 Palaiseau Cedex, France

D. Mailly, X. Lafosse, and C. Ulysse

Laboratoire de Photonique et Nanostructures, CNRS, Marcoussis, France

E. A. Dawi

Debye Institute for Nanomaterials, Nanophotonics Section, Utrecht University, P.O. Box 80000, 3508 TA Utrecht, The Netherlands

The ion-beam-shaping mechanism is studied for several classes of nearly monodispersed metallic nanoparticles (Au, Ag, and $Au_{0.5}Ag_{0.5}$). They are in the range of 3–100 nm and embedded within a silica matrix. Experimentally, we show that depending on their initial sizes, several final morphologies can be obtained: (i) spherical shapes, (ii) facetted nanoparticles, (iii) nanorods, and (iv) nanowires. In parallel, the thermal-spike model was implemented for three-dimensional anisotropic and composite media to study the evolution of the temperature profile within a nanoparticle. This way, a clear correlation is found between the deformation path followed by the nanoparticles during the irradiation and the fraction of the nanoparticle that is molten (vaporized) due to the interaction with a swift heavy ion. This allows the construction of a size-vs-shape diagram relating the initial nanoparticle size to its final morphology. This diagram is used to give a rational description of the ion-beam-shaping process for all nanoparticle dimensions as a function of the irradiation parameters.
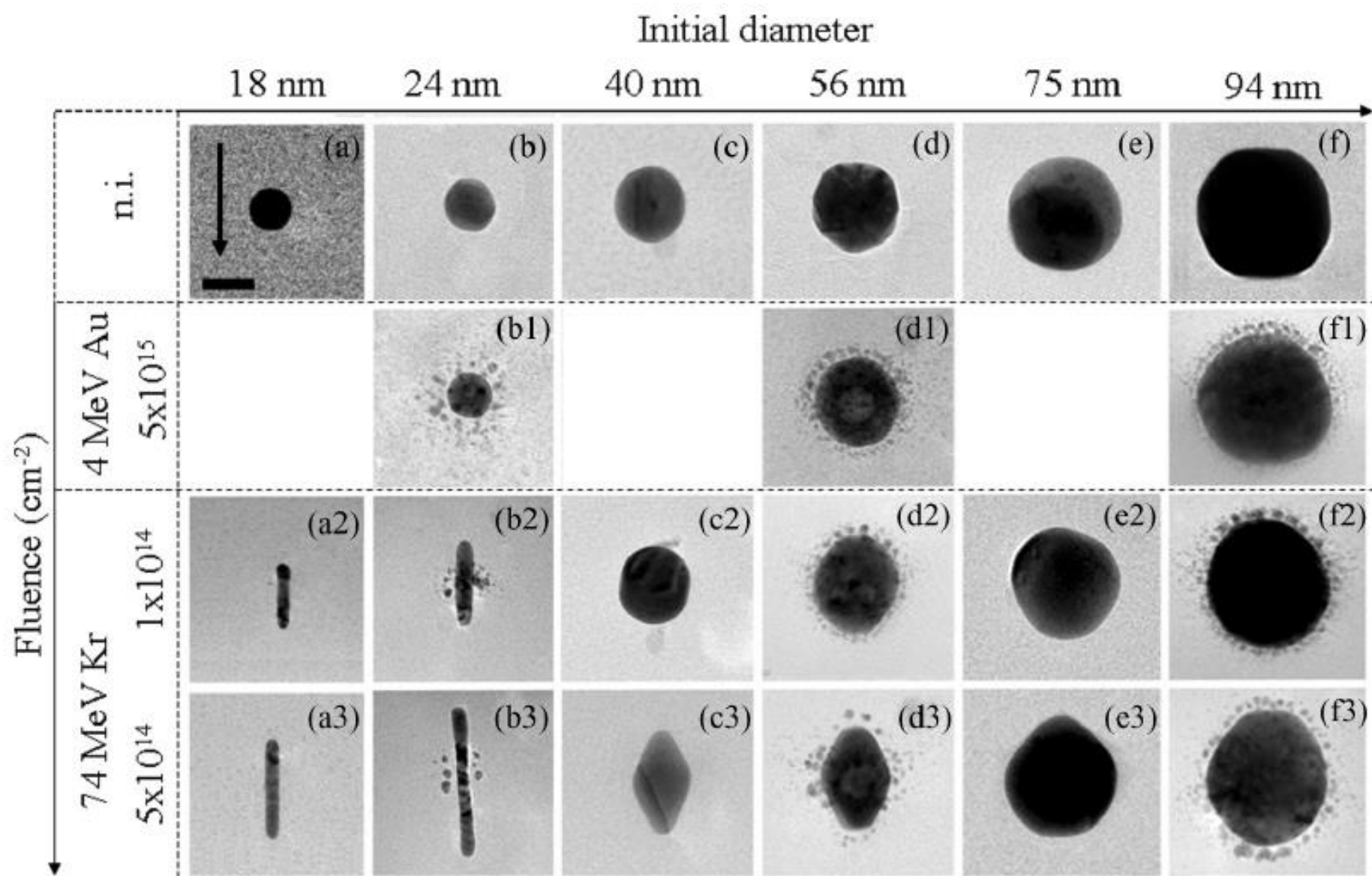
FIG. 1. Matrixlike diagram showing the morphological evolution of Au NPs for increasing initial size (x axis) and irradiation fluence (y axis). The length of the scale bar is 20 nm. The ion-beam direction is indicated by the arrow. Some of the samples [(b1), (d1), and (f1)] have been preirradiated with 4-MeV Au ions at 5×10^{15} cm^{-2} to create a halo of satellites around the central NPs (a2) to (f3). Afterward, all the samples have been irradiated up to 5×10^{15} cm^{-2} with 74-MeV Kr ions.

TABLE I. Thermodynamic parameters. g is the electron-phonon coupling, K_e is the electronic thermal conductivity, N_{at} is the atomic density, E_m is the melting energy, and S_e is the electronic stopping power.

Element	g (W cm^{-3} K^{-1})	K_e (W cm^{-1} K^{-1})	N_{at} (10^{22} cm^{-3})	E_m (eV at^{-1})	S_e (keV nm^{-1}) for Kr ions of various energies in MeV						
					10	25	50	74	100	150	250
Au	2.3×10^{10}[a]	2.8[c]	5.90	0.433	6.9	14.4	22.0	26.3	28.3	30.7	32.7
Ag	3.3×10^{10}[a]	3.8[c]	5.86	0.385	6.4	13.0	19.2	22.1	23.3	24.2	24.7
Au$_{0.5}$Ag$_{0.5}$	2.8×10^{10}	3.3	5.88	0.409	6.6	13.7	20.6	24.2	25.8	27.5	28.7
SiO$_2$	2.2×10^{13}[b]	$3 \times 10^{-5}\, T_e$	$T_e < 7 \times 10^4$ K	(see Ref. 14)	3.6	6.5	8.5	9.2	9.6	9.9	10.0
SiO$_2$		2.0	$T_e > 7 \times 10^4$ K								
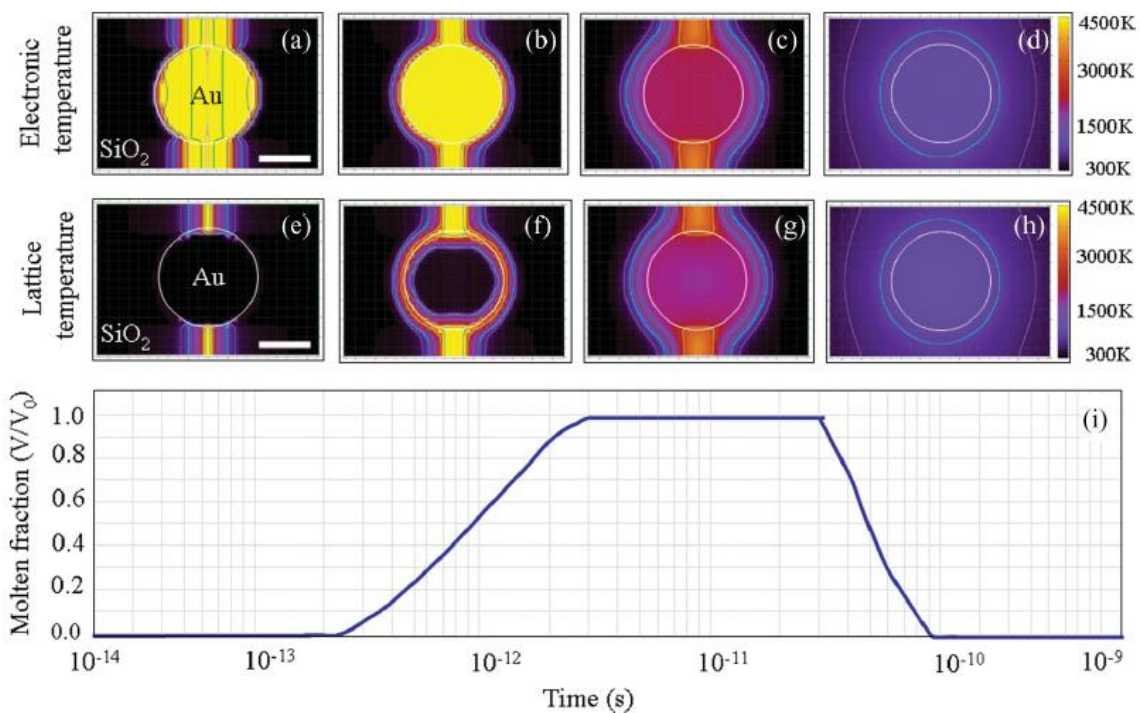
FIG. 4. (Color online) Timeline of the thermal evolution for a 20-nm Au NP embedded within a SiO$_2$ matrix irradiated with a 74-MeV Kr ion. Simulations have been run considering an ion intercepting the NP at the pole. (a)–(d) electronic temperature and (e)–(h) lattice temperature. (i) Time evolution of the fraction of the NP that reaches a temperature larger than that of melting, i.e., the molten fraction.
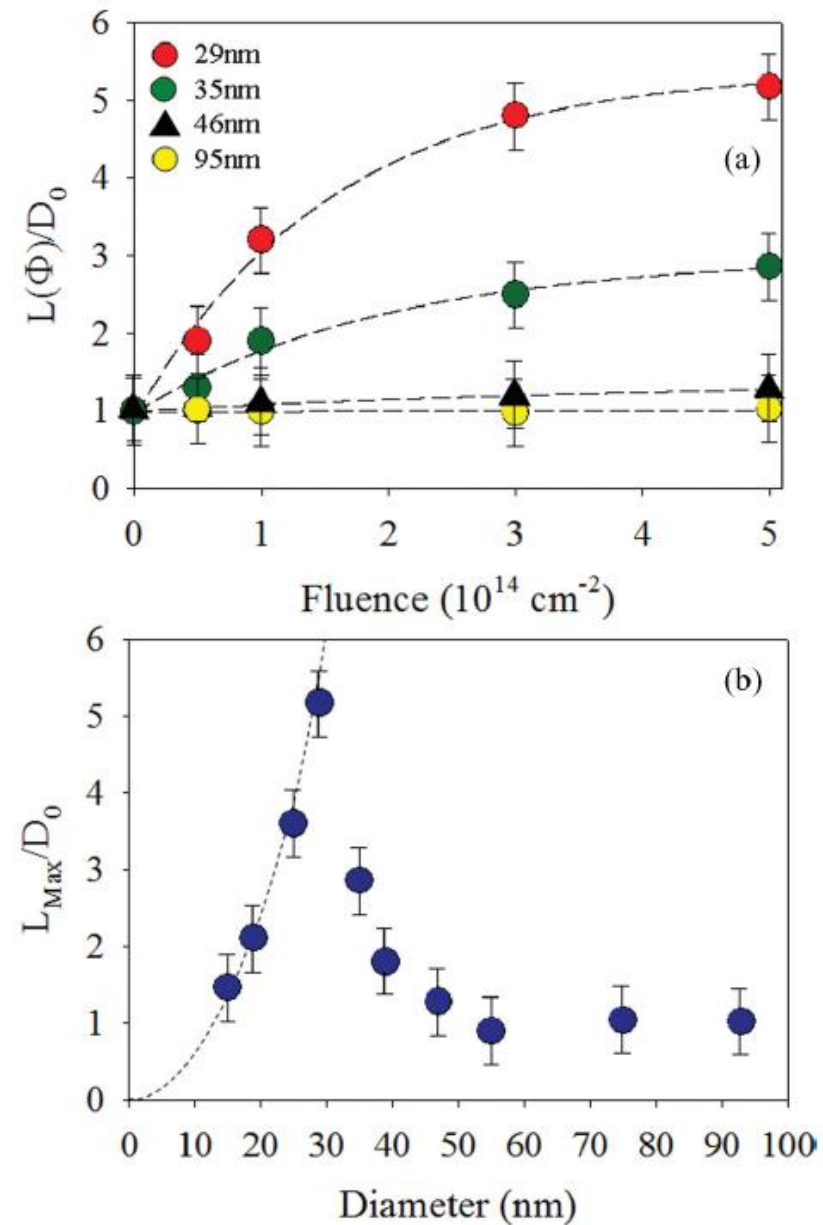
FIG. 3. (Color online) (a) Evolution of the normalized major axis $L(\Phi)/D_0$ as a function of the irradiation fluence Φ. (b) Evolution of the normalized maximum deformation length (L_{max}/D_0), obtained at a fluence of 5×10^{14} cm^{-2}, as a function of the initial NP size, D_0.
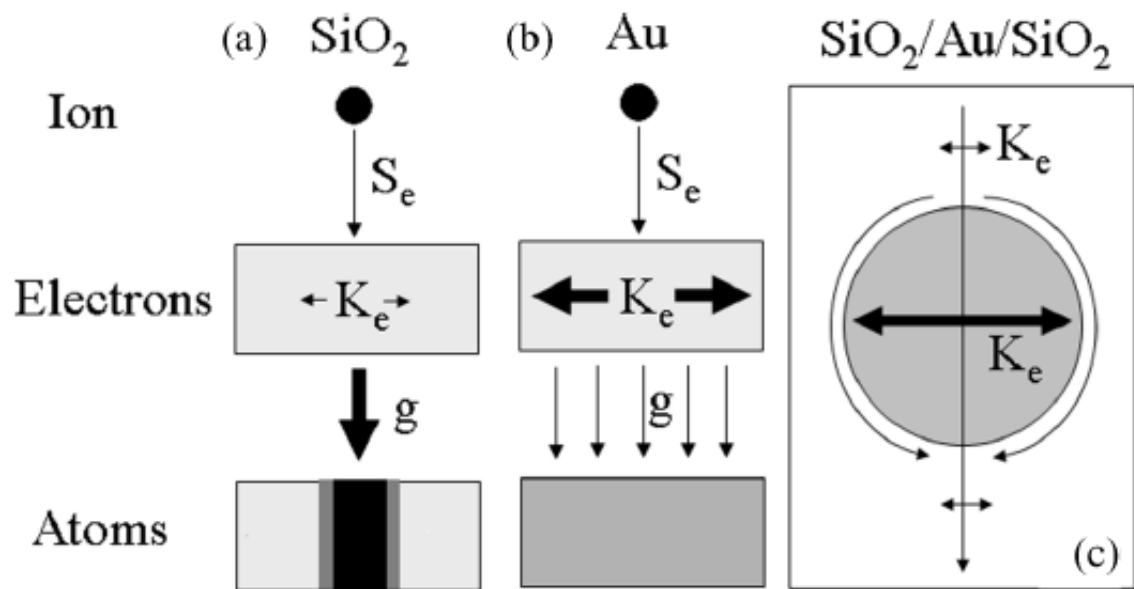
FIG. 5. Schematic diagram for the swift-heavy-ion–matter interaction for (a) bulk silica, (b) bulk gold, and (c) gold NPs confined within a SiO_2 matrix.
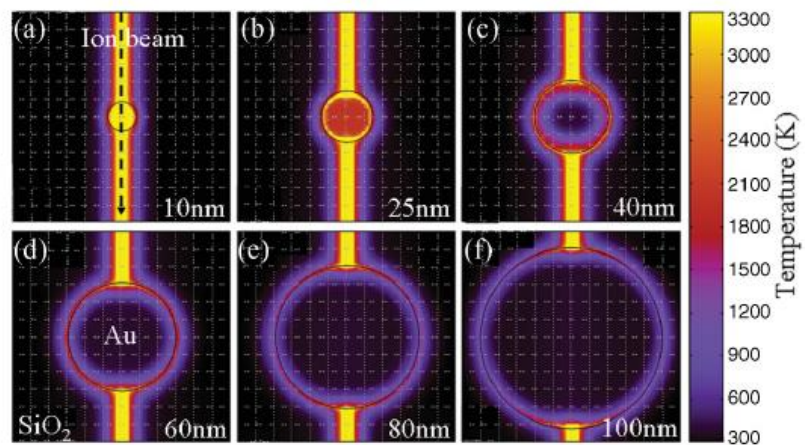

FIG. 6. (Color online) Each panel represents the 3D-TS simulation corresponding to the highest temperature reached within the Au NPs. The ion trajectory is indicated by the dotted arrow. The sizes of the NPs are (a) 10 nm, (b) 25 nm, (c) 40 nm, (d) 60 nm, (e) 80 nm, and (f) 100 nm.
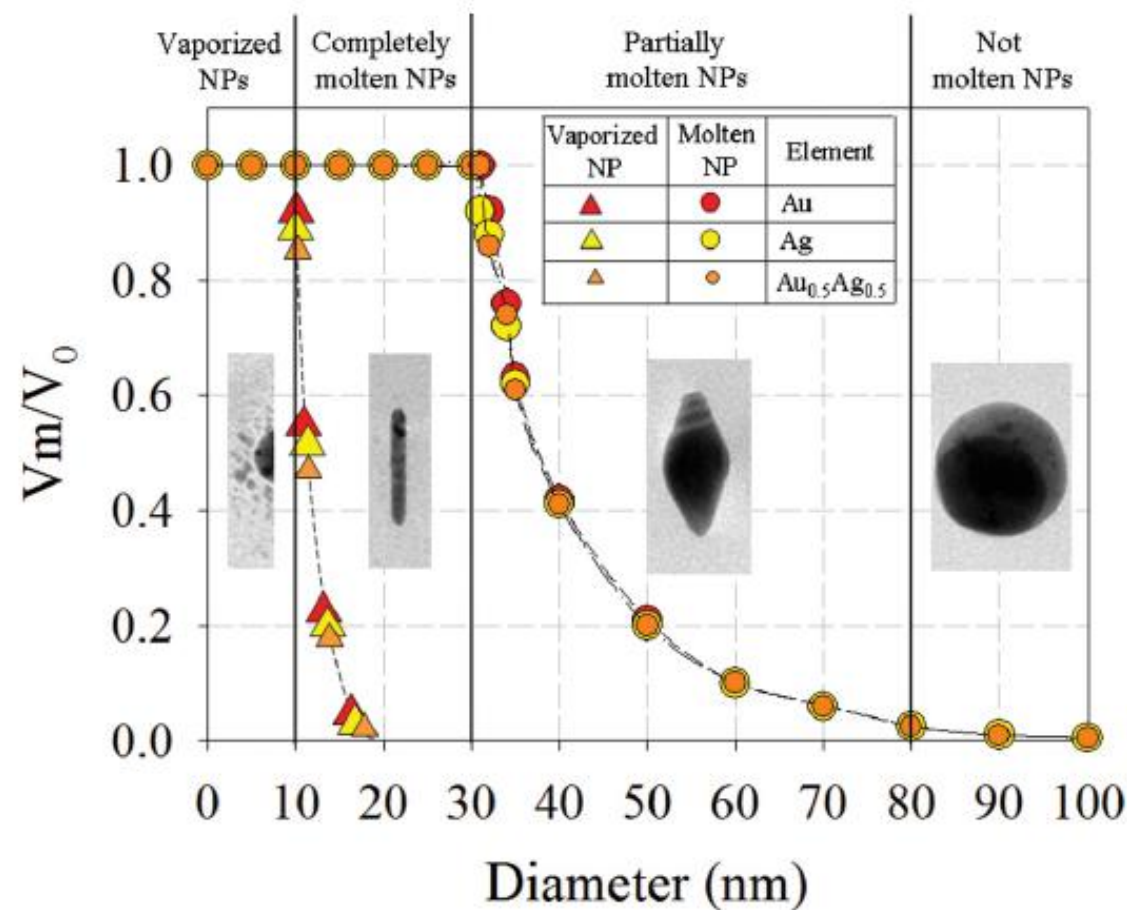

FIG. 7. (Color online) The size-vs-shape diagram used to rationalize the ion-beam-shaping process for all the NP sizes. Four temperature-dependent regions can be defined: (i) vaporized NPs (1–10 nm) conserve their spherical shape, (ii) completely molten NPs (10–30 nm) transform into nanorods and/or nanowires, (iii) partially molten NPs (30–80 nm) evolve toward faceted NPs, and (iv) not molten NPs (>80 nm) do not deform, or their deformation rate is very low. The vaporized fraction is represented by triangles whereas the molten fraction is represented by circles.
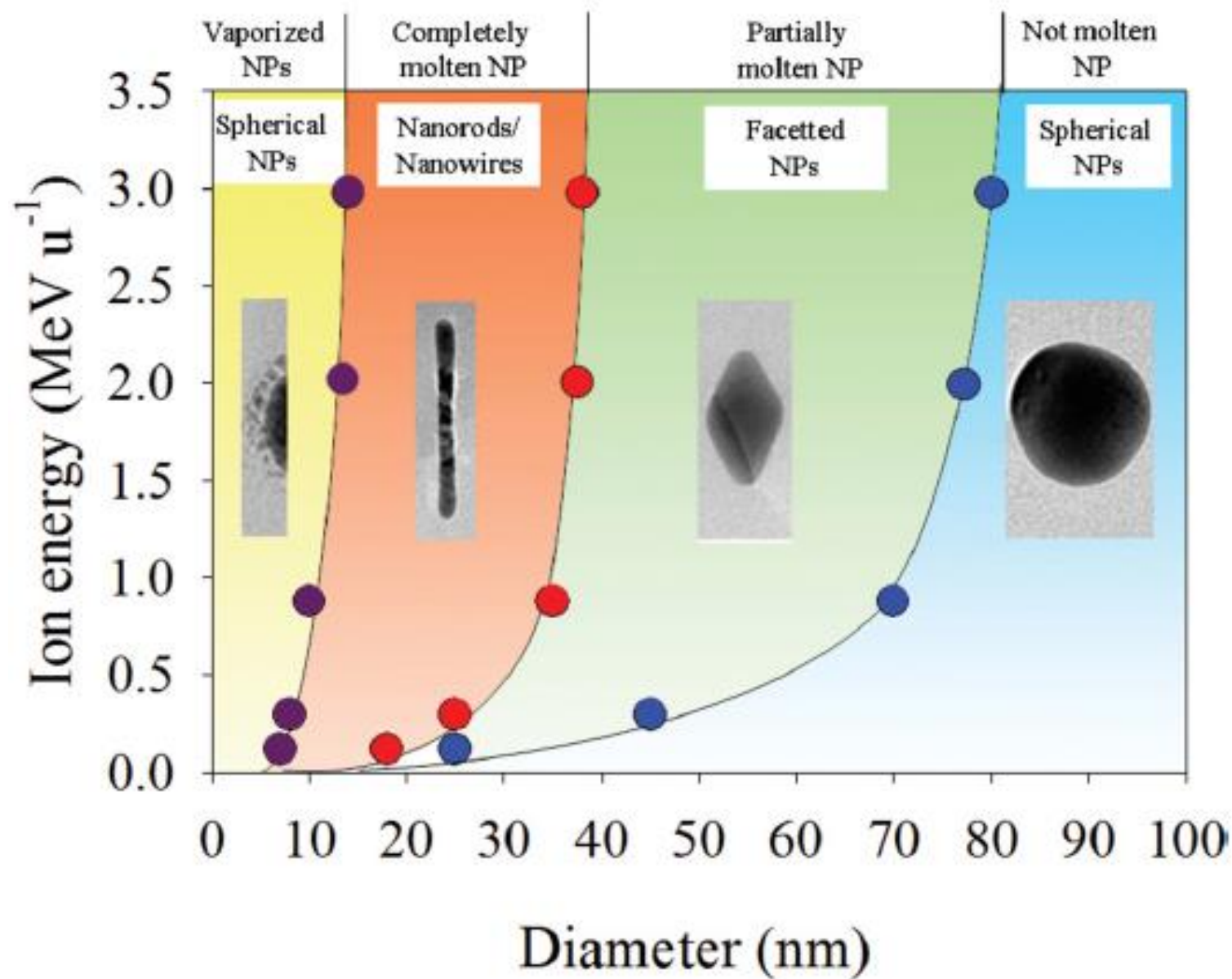
FIG. 11. (Color online) Evolution of the size-vs-shape diagram when both the NP size and the ion energy are varied.

Ion beam irradiation of embedded nanoparticles: Toward an *in situ* control of size and spatial distribution

G. Rizza[a)] and H. Cheverry
Laboratoire des Solides Irradiés, Ecole Polytechnique/CEA-DRECAM/CNRS, 91128 Palaiseau Cedex, France

T. Gacoin and A. Lamasson
Groupe de Chimie du Solide, Laboratoire de Physique de la Matière Condensée, UMR CNRS 7643, Ecole Polytechnique, 91128 Palaiseau, France

S. Henry
Centre de Spectrométrie Nucleaire et de Spectrométrie de Masse, CNRS-IN2P3, Bât 108, 91405 Orsay, Campus, France

Irradiation of chemically synthesized Au nanoparticles embedded in a dielectric matrix promotes the formation of a halo of satellites around the original cluster. We show that the complete dissolution of the nanoparticles (NC) results in the formation of a narrow size distribution of small precipitates with a mean size of 2 nm and a standard deviation of 0.4 nm. By combining the chemical synthesis of the nanoparticles and the irradiation to induce their dissolution and precipitation, we give a guideline method for overcoming the difficulty of controlling the size and spatial distribution of the embedded NC associated with ion implantation technique. In particular, we showed that the irradiation can be used to tailor the size of the already formed NC. Moreover, we establish that the satellites cluster evolution under irradiation can be described by a two step process. These two steps are discussed in terms of classical and inverse Ostwald ripening mechanisms. © 2007 American Institute of Physics. [DOI: 10.1063/1.2402351]
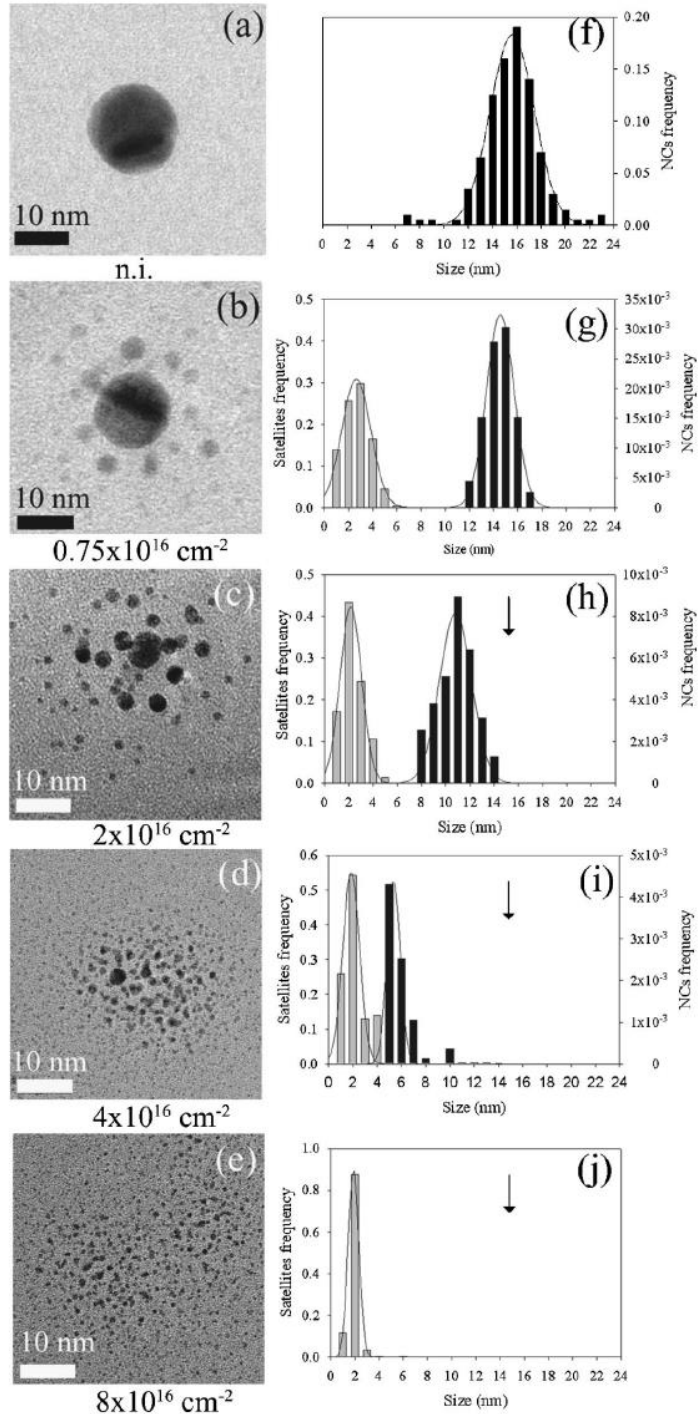
FIG. 1. (a)–(e) Bright field TEM micrographs of the time sequence of NC evolution under 4 MeV Au irradiation at 300 K. The samples were irradiated at increasing fluences up 8×10^{16} cm^{-2}. (f)–(j) The corresponding size distributions of NC and satellites.
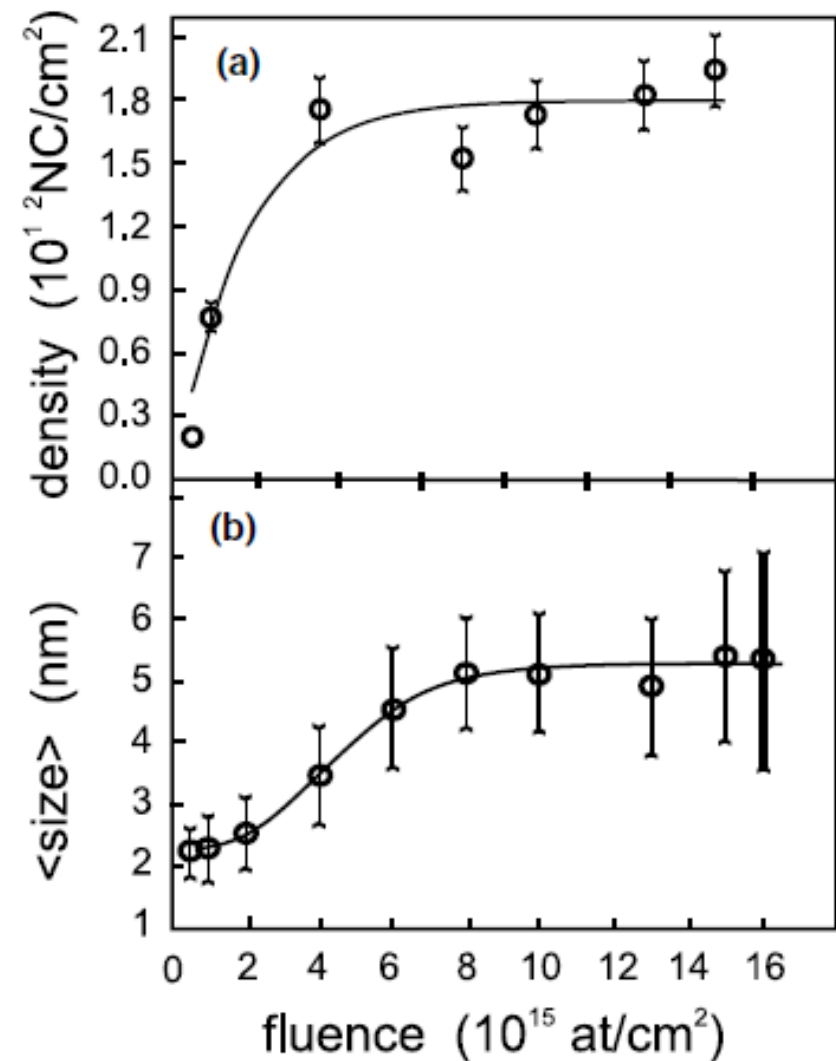

Fig. 2. Density (a) and size (b) evolution of nanoclusters around large inclusions during room temperature ion beam mixing with Au ions at 4.5 MeV at an ion flux of 10^{12} Au cm^{-2} s^{-1}. Saturation occurs at high irradiation fluences, showing that a steady-state regime is reached.

Ion irradiation of gold inclusions in SiO$_2$: Experimental evidence for inverse Ostwald ripening

G.C. Rizza [a,*], M. Strobel [b], K.H. Heinig [b], H. Bernas [a]

[a] Centre de Spectrométrie Nucléaire et de Spectrométrie de Masse, CNRS-IN2P3, Bat. 108, 91405 Orsay, Campus, France
[b] Institute of Ion Beam Physics and Materials Research, Forschungzentrum Rossendorf, P.O. Box 510 119, D-01314 Dresden, Germany

Abstract

When sub mm size gold inclusions in SiO$_2$ are irradiated with MeV gold ions, a ring of nanometer-size clusters is formed in their immediate vicinity. The size, density and radial distribution of these nanoclusters were determined. Our observations are in agreement with a recent prediction that in a driven system, under appropriate ion beam and temperature conditions, the steady-state solute concentration's dependence on precipitate size may be opposite to that expected from the equilibrium Gibbs–Thomson relation. Kinetic Monte-Carlo simulations account for additional experimental results: the irradiation-induced increase in solute concentration can promote nucleation of additional precipitates around the first ring. The latter finding contradicts the usual assumption that ion beam mixing hinders nucleation. © 2001 Elsevier Science B.V. All rights reserved.
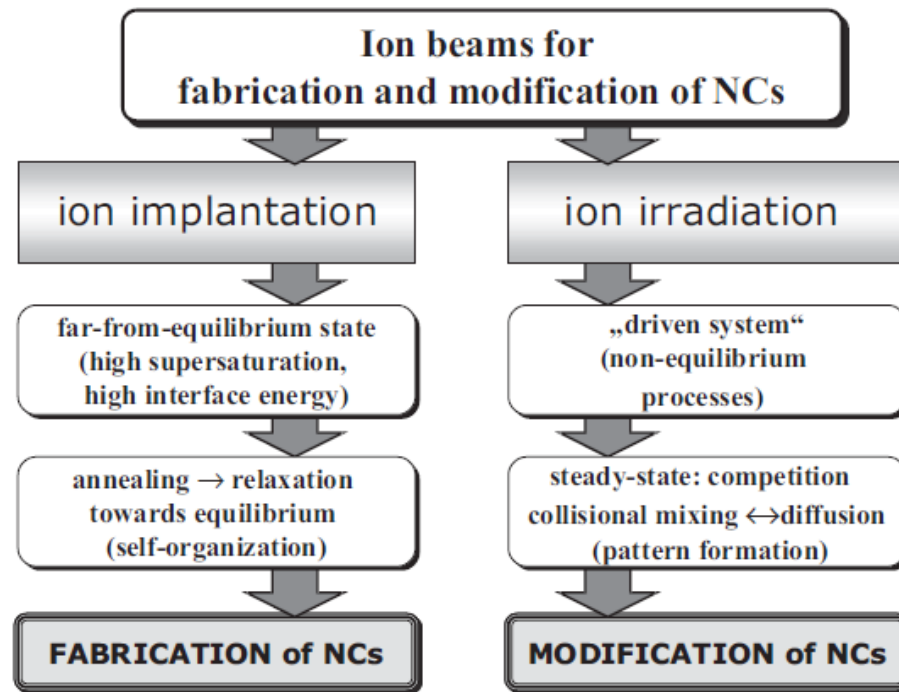
Interfaces under ion irradiation: growth and taming of nanostructures

K.H. HEINIG✉

T. MÜLLER

B. SCHMIDT

M. STROBEL

W. MÖLLER

Institute of Ion Beam Physics and Materials Research, Research Center Rossendorf, PSF 51 01 19, 01314 Dresden, Germany

FIGURE 1 Two regimes of fabrication and modification of NCs with ion beams. By ion implantation, a surface layer is transferred into a highly supersaturated, far-from-equilibrium state. NC formation happens by phase separation, where self-organization may occur. In contrast, ion irradiation of NCs embedded in a surface layer brings them into a steady state far from equilibrium, where a competition between collisional mixing and diffusion may result in pattern formation

ABSTRACT We have investigated the synthesis of nanostructures, as well as the control of their size and location by means of ion beams. The phase separation and interface kinetics under ion irradiation give new possibilities for controlling the growth of nanostructures. Additionally, the chemical decomposition of the host matrix by collisional mixing can contribute to the self-organization of nanostructures, especially at interfaces. It is shown how collisional mixing during ion implantation affects nanocrystal (NC) synthesis and how ion irradiation through NCs modifies their size and size distribution. An analytical expression for solute concentration around an ion-irradiated NC was found, which may be written like the well-known Gibbs–Thomson relation. However, parameters have modified meanings, which has a significant impact on the evolution of NC ensembles. "Inverse Ostwald ripening" of NCs, resulting in an unimodal NC size distribution, is predicted, which has been confirmed experimentally for Au NCs in SiO_2 and by kinetic lattice Monte Carlo simulations. At interfaces, the same ion-irradiation-induced mechanism may result in self-organization of NCs into a thin δ-layer. Collisional decomposition of SiO_2 may enhance the NC δ-layer formation in SiO_2 at the Si/SiO_2 interface. The distance of the self-organized NC δ-layer from the SiO_2/Si interface renders the structure interesting for non-volatile memory applications.

displaced atom

ρ

a

nanocluster of radius R_o

δ

R_{cl}

R

$R-r$

λ

r

0

b
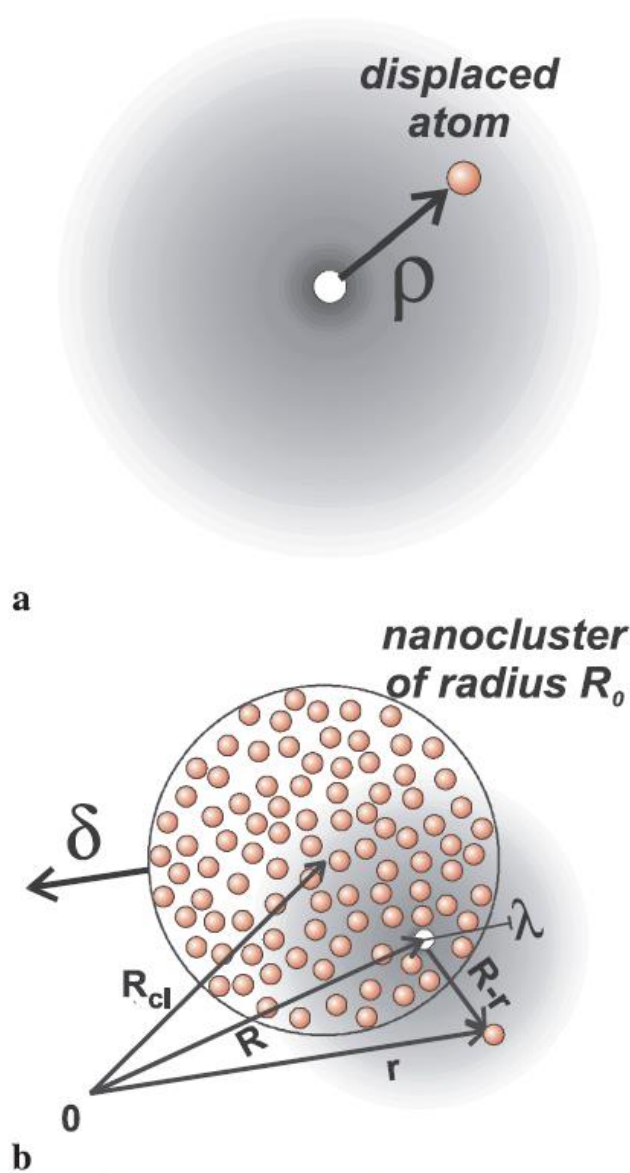
FIGURE 5   An atom, originally located at $\varrho = 0$, is displaced isotropically in any direction by a collision with a recoil of the collision cascade, and comes to rest at ϱ [24]. The displacement probability $f(\varrho) \propto \exp[-\varrho/\lambda]$ refers to the average of displacements by all recoils of the full collision cascade (a). The number of atoms displaced out of a NC into the host matrix is obtained by an integration of $f(R-r)$ of the atoms located at the space coordinate R in the NC (b). Here, R_{cl} is the location of the center of the NC

Before the steady-state concentration of a NC under ion irradiation will be calculated, it should be mentioned that in thermal equilibrium (without ion irradiation) the solute concentration around a spherical NC of radius R_0 is given by the Gibbs–Thomson relation:

$$C(R_0) = C_\infty \times (1 + R_c/R_0), \tag{1}$$

where C_∞ is the solubility at a flat interface and R_C is the capillary length.

The starting point of the analytical treatment of the steady-state behavior of NCs under ion irradiation is the spatial probability distribution $f(\varrho)$ of atomic displacements caused by a collision cascade, as illustrated in Fig. 5a. $f(\varrho)$ is given to a good approximation by $f(\varrho) \propto \exp[-\varrho/\lambda]$, where ϱ is the distance of the displaced atom from its original position and λ is the mean displacement distance. The spatial probability distribution $W_{R_0}(r)$ of atoms displaced out of a NC is obtained by a superposition of the displacement probabilities of all atoms in a NC (see Fig. 5b). The integration over five space coordi-

The starting point of the analytical treatment of the steady-state behavior of NCs under ion irradiation is the spatial probability distribution $f(\varrho)$ of atomic displacements caused by a collision cascade, as illustrated in Fig. 5a. $f(\varrho)$ is given to a good approximation by $f(\varrho) \propto \exp[-\varrho/\lambda]$, where ϱ is the distance of the displaced atom from its original position and λ is the mean displacement distance. The spatial probability distribution $W_{R_0}(r)$ of atoms displaced out of a NC is obtained by a superposition of the displacement probabilities of all atoms in a NC (see Fig. 5b). The integration over five space coordi-

The steady-state solute concentration around a NC is obtained from the diffusion equation

$$D\frac{1}{r^2}\frac{\partial}{\partial r}\left(r^2\frac{\partial}{\partial r}C(r)\right) = \Phi W_{R_0}(r - R_0), \tag{4}$$

$$C^I(R_0) = C_\infty^I \left(1 + R_c^I/R_0\right) \text{ with}$$
$$C_\infty^I = C_\infty (1 + \Delta)$$
$$R_c^I = (R_c - 5\lambda\Delta/4) / (1 + \Delta)$$
$$\Delta = q\Phi\lambda^2/DC_\infty \tag{5}$$

with $q\Phi$ being the damage rate.

With the result of (5), it is proven that for thermal treatment both with and without ion irradiation, the impurity concentration around a nanocluster obeys a similar law in the form of the Gibbs–Thomson relation (see (1)). However, under ion irradiation the solubility C_∞^I and capillary length R_c^I are modified.
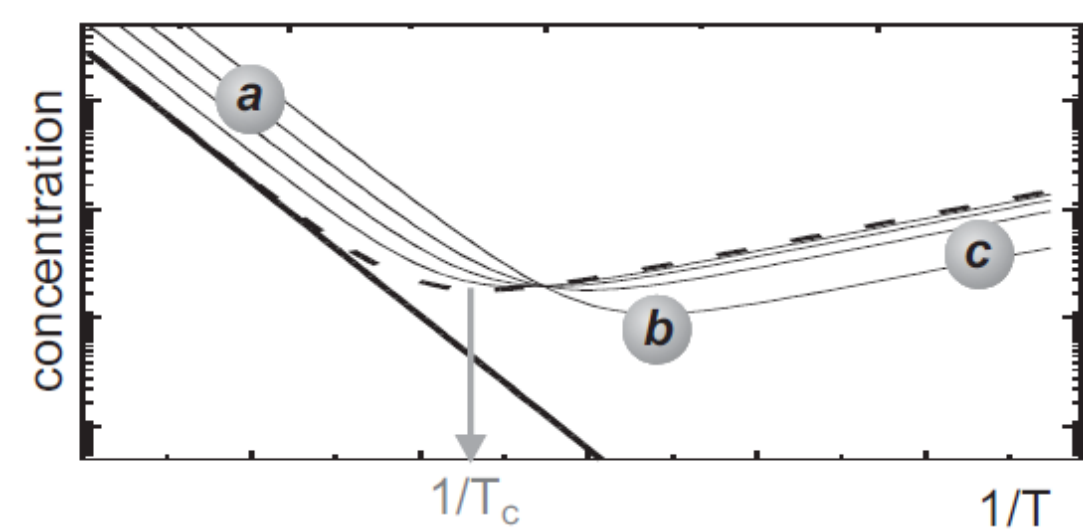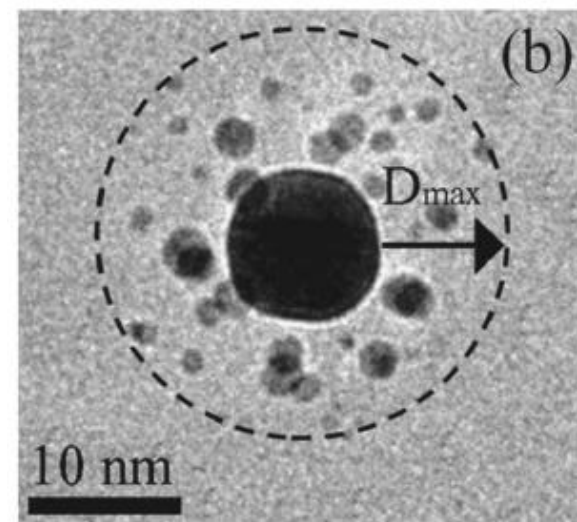
FIGURE 7 Dependence of the steady-state solute concentration $C^I(R_0, T)$ around a NC on the sample temperature T during ion irradiation, as predicted by (5). The *thick solid line* shows the usual solubility (solidus). The *thick dashed curve* is the steady-state solute concentration under ion irradiation. The *thin solid curves* are the steady-state solute concentrations of ion-irradiated NCs of 1.5, 2, 4 and 10 nm size (curves are more distant from the dashed curve for smaller NCs). The curves are plotted for $CoSi_2$ NCs in Si [33], where numbers have been omitted to underline the general behavior
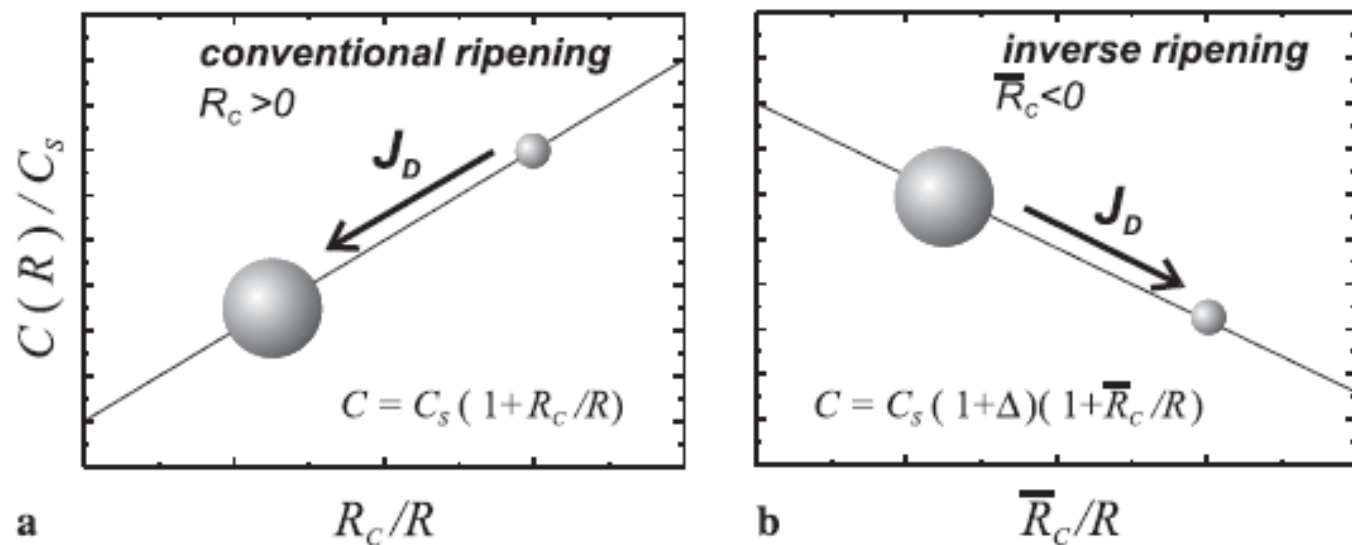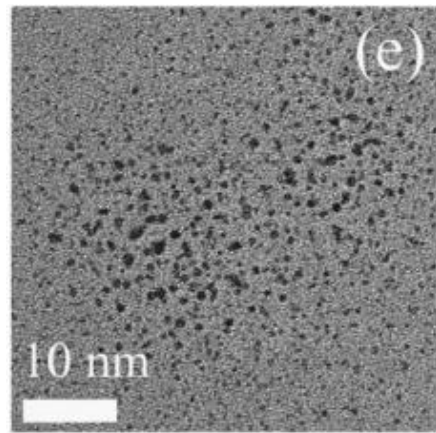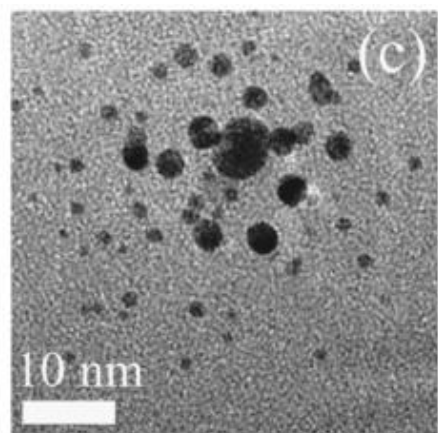
FIGURE 8 Dependence of the steady-state solute concentration $C(R)$ around a NC on the radius R of the NC. For a positive capillary length R_c the usual behavior resulting in conventional Ostwald ripening is found (**a**). If R_c in (5) becomes negative under ion irradiation, then small NCs grow at the expense of large ones (**b**). Inverse Ostwald ripening will be observed

Embedding of metal nanoparticles in polymeric matrices

1) INTRODUCTION

➤ **A) Metal/Polymer nanocomposites: properties and applications**

Metal nanoparticles

$\sim$ nm

- Quantum size effects,
- Plasmonic properties,
- Reactivity,
- ……..

Polymer films

Polymeric chains

- Flexibility,
- Trasparency,
- Phase transitions,
- ……..

Tuning the metal/polymer interaction to tune the physical properties

- *Strong (covalent attachment)*
- *Weak (physical absorption)*

➤ *Lightweight*
➤ *High mechanical properties*
➤ *Unique physical properties*
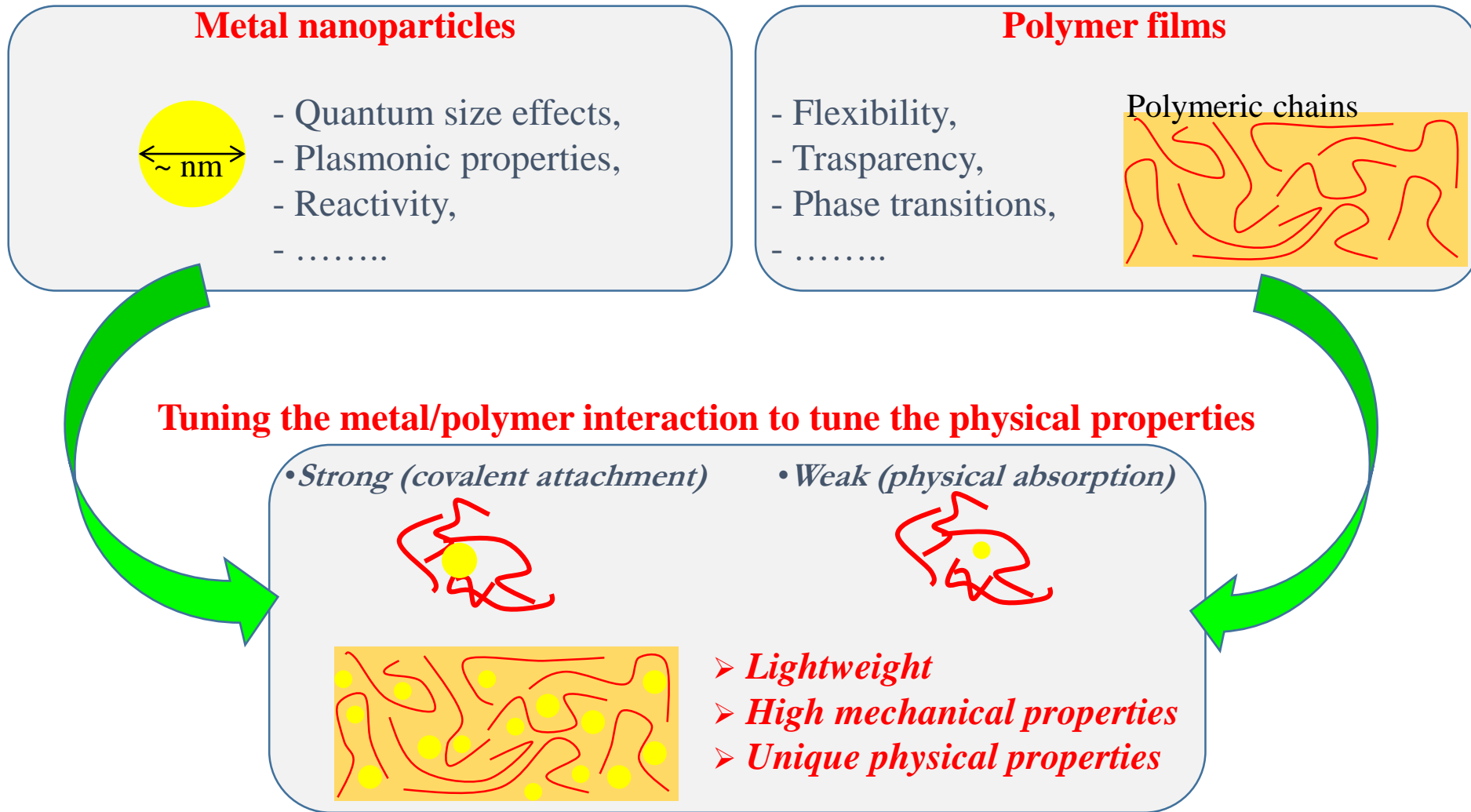
Metals undergo the most considerable properties change by size reduction, and their composites with polymers are very interesting for **functional applications** because the properties of nano-sized metals (optical, magnetic, dielectric, electrical and thermal transport properties) leave unmodified after embedding in polymers.

L. Nicolais, G. Carotenuto (Eds), «Metal-Polymer nanocomposites», Wiley (2005).

Polymer matrix	Nanoparticle	Application (Reference)
Polyaniline	Gold	Sensor (Paul and Robeson, 2008)
Natural rubber	Silver	Latex gloves (Paul and Robeson, 2008)
PET	Silver	Bandpass filter (Avasthi et al., 2007)
Polypyrrole	Platinum	Fuel cell (Malinauskas et al., 2005)
Poly(vinyl chloride)	Copper	Biotechnology (Cioffi et al., 2005)
Polyaniline	Copper	Sensor (Sharma et al., 2002)
Polytetrafluoroethylene	Silver	Optical filler/sensor (Schurmann, 2005)
PEDOT: PSS	Silver/gold	Electrochromic device (Namboothiry, 2007)
Bisphenol A	Silver	Capacitor (Pothukuchi et al., 2004)
Polydimethylsiloxane	Gold	SERS (Giesfeldt et al., 2005)
PANI-PSS	Platinum	Fuel cell (Liu et al., 2007)
Polysulfone	Platinum	Sensor (Muraviev et al., 2006)
Polymethylmethacrylate	Gold	Sensor (Hanisch et al., 2008)

O. M. Folarin et al., «Polymer-noble metal nanocomposites: Review», Int. J. Phys. Sci. 6, 4869 (2011)
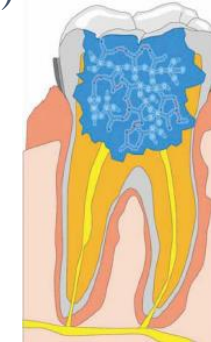
Only some examples:
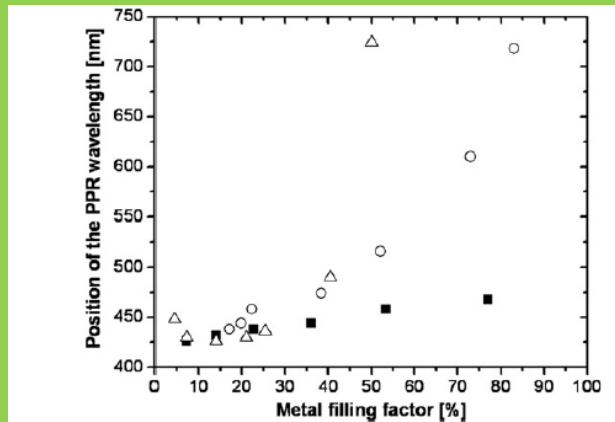
Figure 7. Position of the PPR wavelength versus the metal filling factor for: ■, Ag/TAF; O, Ag/PMMA; △, Ag/Nylon.

H. Takele et al., «Plasmonic properties of Ag nanoclusters in various polymer matrices», Nanotechnology 17, 3499 (2006)

H. Takele et al., «Tuning of electrical and structural properties of metal-polymer nanocomposite films prepared by co-evaporation technique», Applied Physics A 92, 345 (2008)
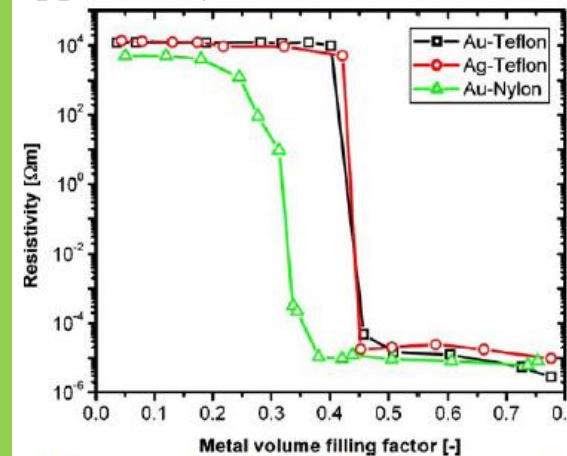
FIGURE 2 Electrical resistivity of Au-Teflon AF, Ag-Teflon AF and Au-Nylon nanocomposites with increasing metal filling factor
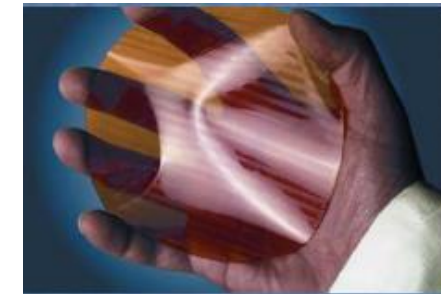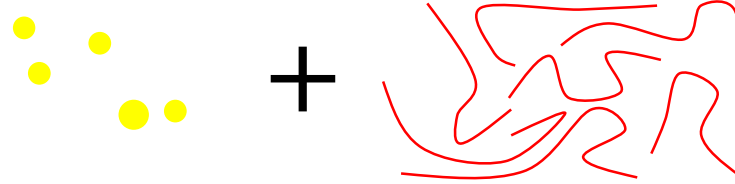
Chemical methodologies

1) **In-situ polymerization,**
2) **Mesophase mediated emulsion,**
3) **Solution-based approaches,**

R. D. Deshmukh,
Z. J. Guo,
J. H. Teichroeb,
………

Physical methodologies

1) **Sequential evaporation,**
2) **Co-evaporation,**
3) **Co-Sputtering,**
4) **Ion implantation.**

V. Zaporojtchenko,
F. Faupel,
Y. K. Mishra,
………

Our aim:
Development of simple, low-cost, large-scale, and versatile processes to fabricate and manipulate metallic (Ag, Au) nanostructures in polymers (PMMA and PS) matrices

2) Embedding kinetics of Au and Ag nanoparticles in PMMA and PS layers

➤ **Au and Ag deposition on PMMA and PS: sputtering**

➤ **Thermal processes above T_g**

➤ **Quantification of the embedding kinetics**

PMMA or PS Spin-coating on Si
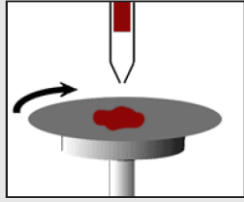
d=200 nm

PMMA or PS

Si

By controlling the deposition parameters <u>d can be tuned</u>

Au or Ag sputtering on PMMA or PS

Au or Ag target

R

By controlling the deposition parameters <u><R> and N can be tuned</u>
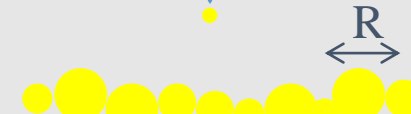
PMMA or PS

Si

Au and Ag average thickness: 10 nm

PS

2 nm
0

250 nm
0

PMMA

2 nm
0

250 nm
0

PMMA ——————————————————————————————————————→

$T_g = 105\ °C$ $T_M = 160\ °C$

PS ——————————————————————————————————————→

$T_g = 95\ °C$ $T_M = 240\ °C$

120-160 °C, 60-180 min   **200-240 °C, 60-180 min**

Au   Ag   Au   Ag

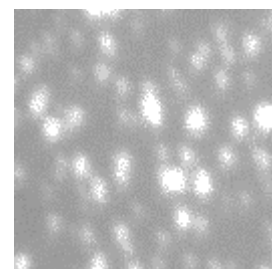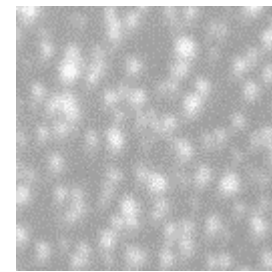| PMMA	PMMA	PS	PS
Si	Si	Si	Si

T < T_g: Solid state system   **T > T_g: Viscous fluid state system**

Phase transition

Long-range chains mobility

Ag/PS

a   e   h   i

250 nm   250 nm   250 nm   250 nm

25 nm   15 nm   10 nm   3 nm
0   0   0   0

0   0   0   0
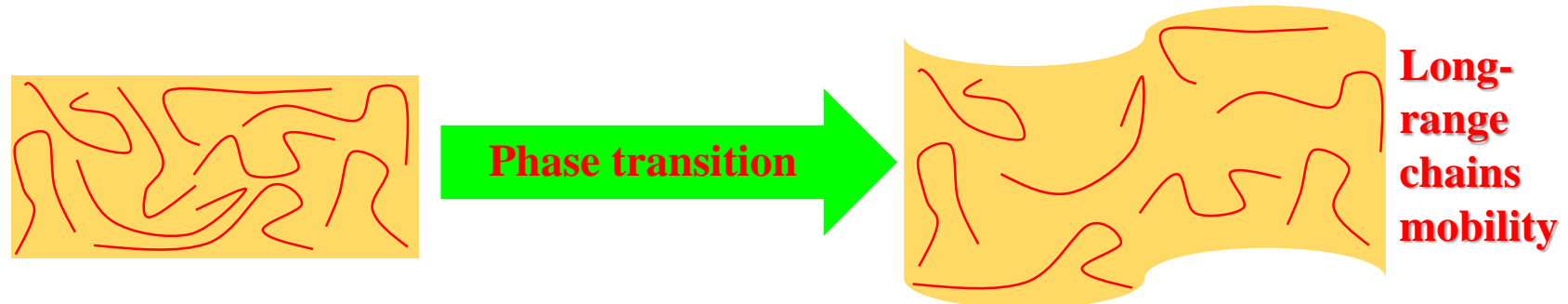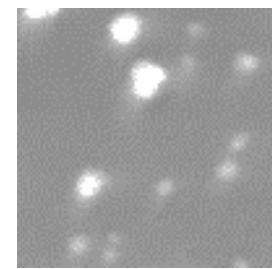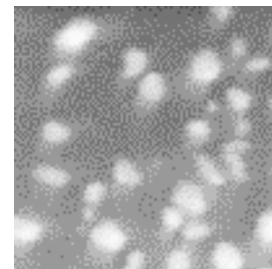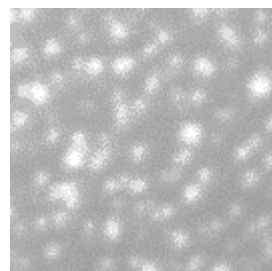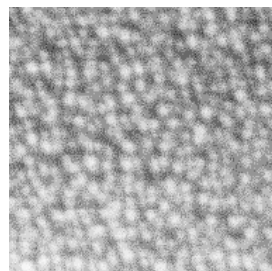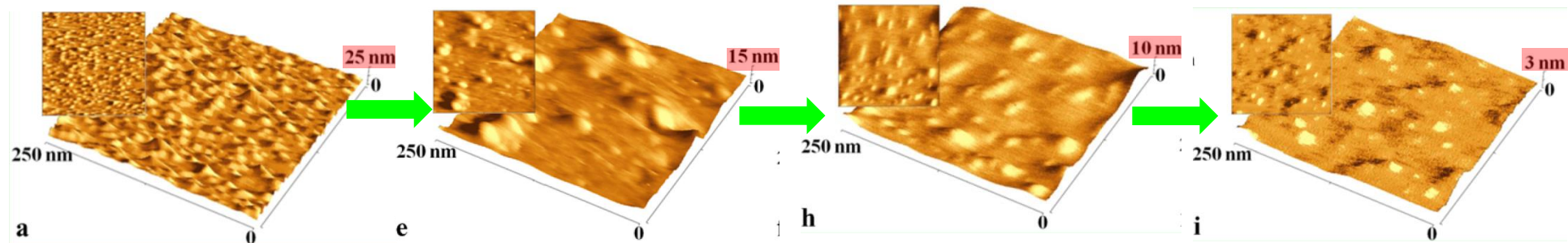
200 °C-1h   220 °C-2h   240 °C-2h   240 °C-3h
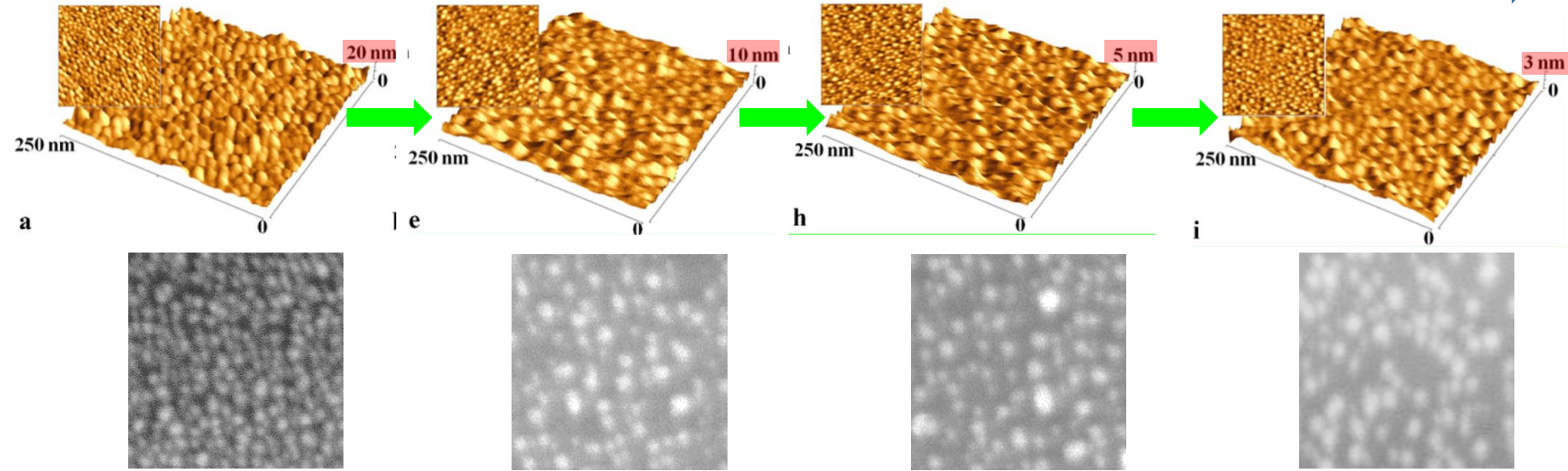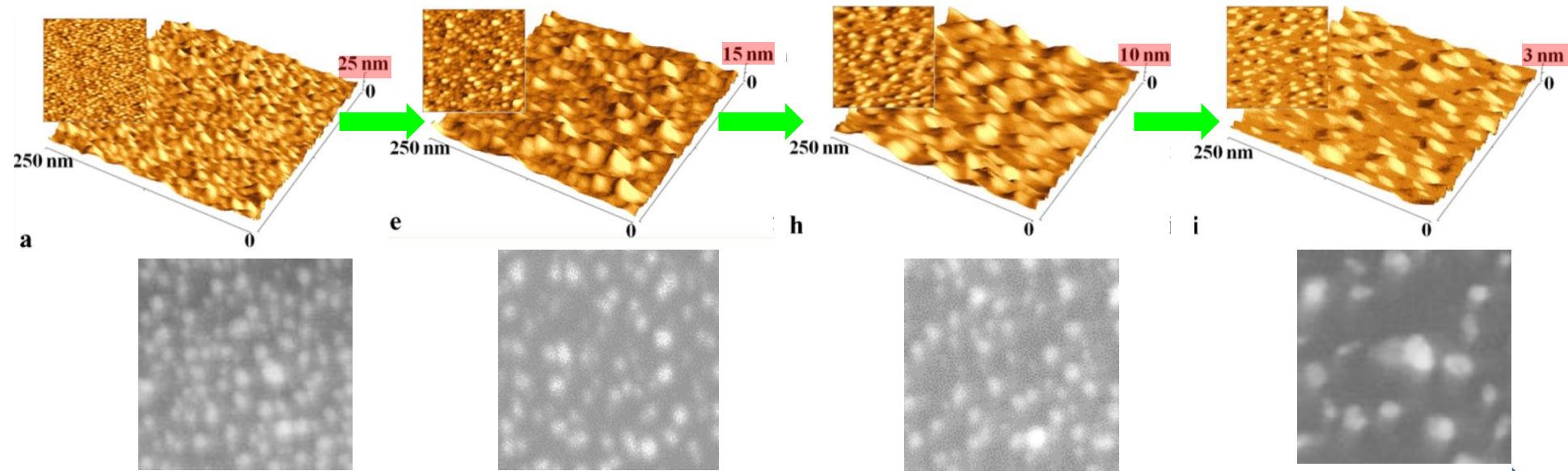
a   e   h   i

250 nm   250 nm   250 nm   250 nm

25 nm   10 nm   5 nm   3 nm
0   0   0   0

0   0   0   0

250 nm

Au/PS

Ag/PMMA

120 °C-1h   140 °C-2h   160 °C-2h   160 °C-3h
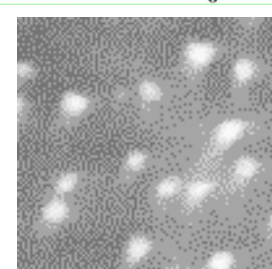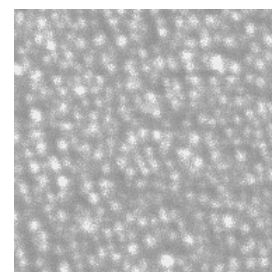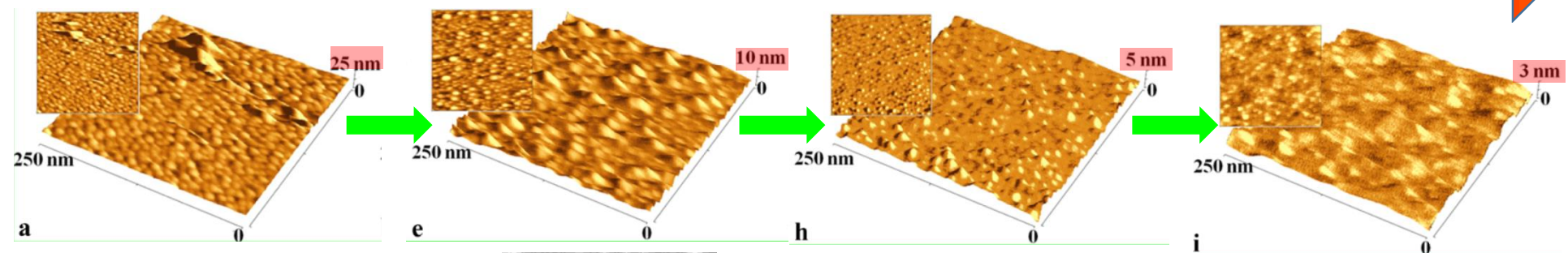
250 nm

Au/PMMA

A) Mean nanoparticles and surface density of disappeared nanoparticles evaluation

Au/PS+513 K

Coating time $t_0=3230$ s

$v=2.3$ Å/min Embedding velocity

Polymer layer
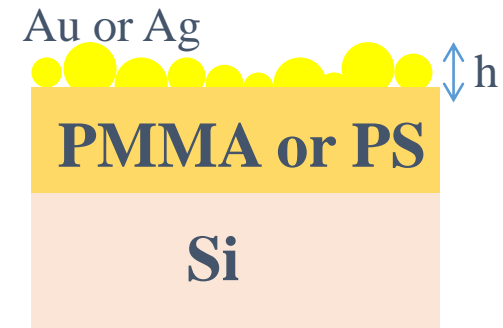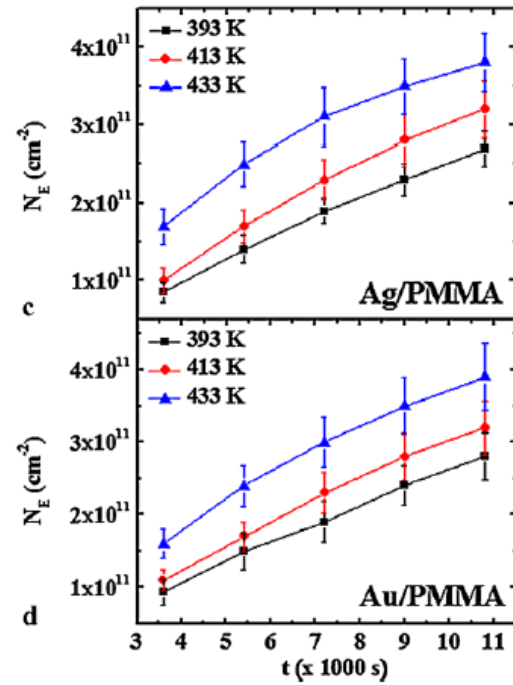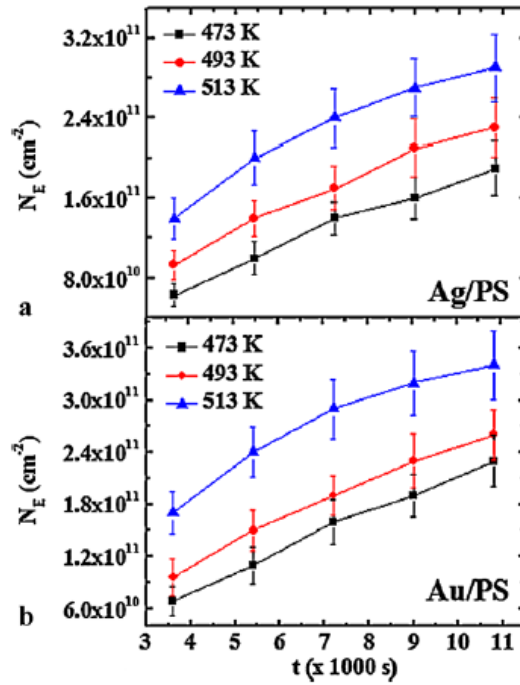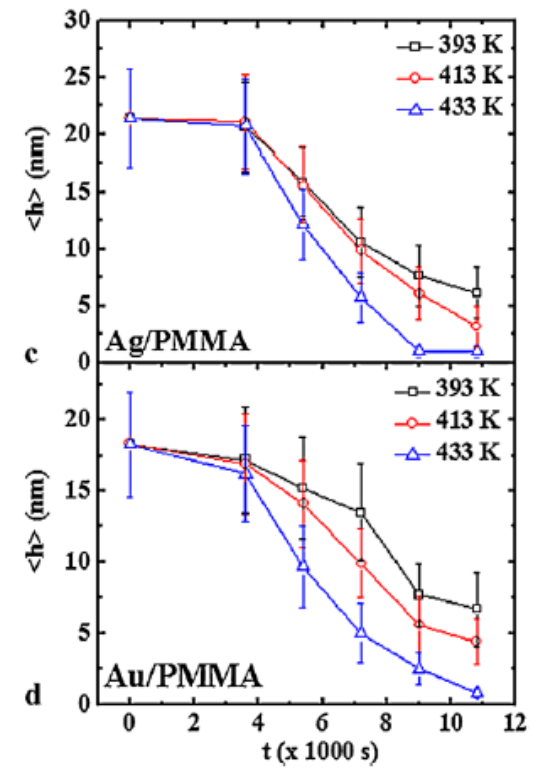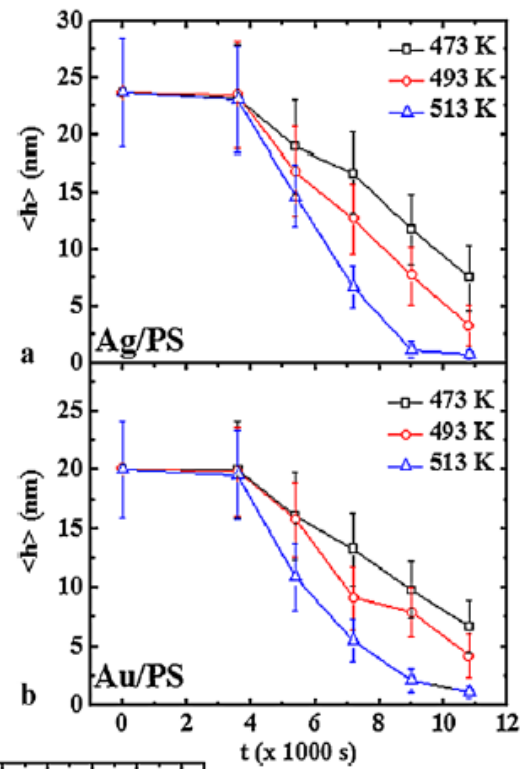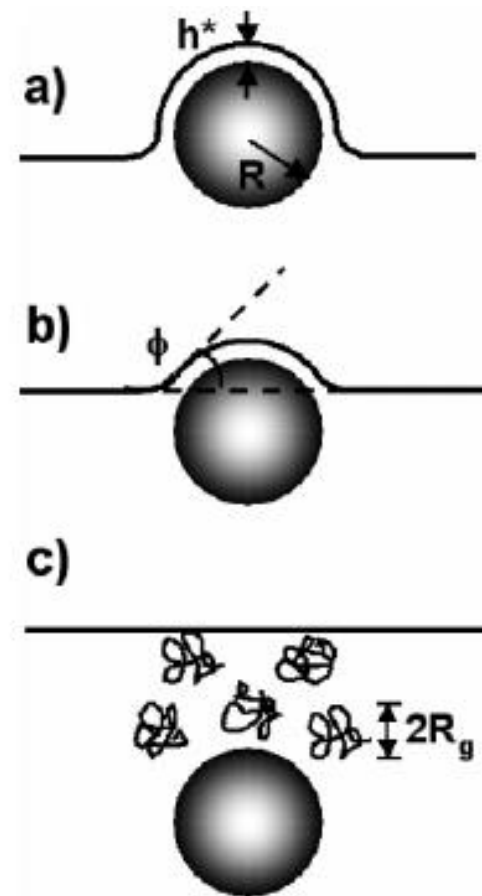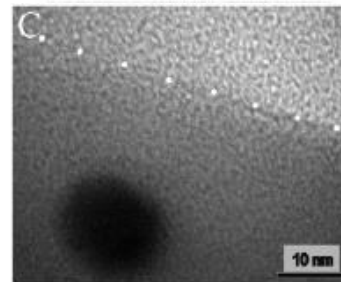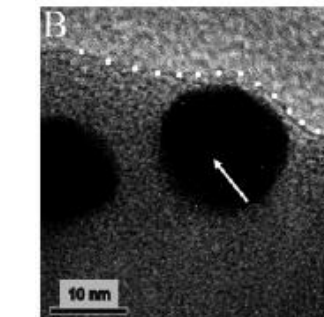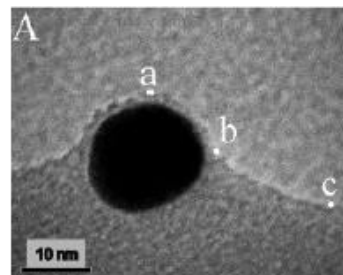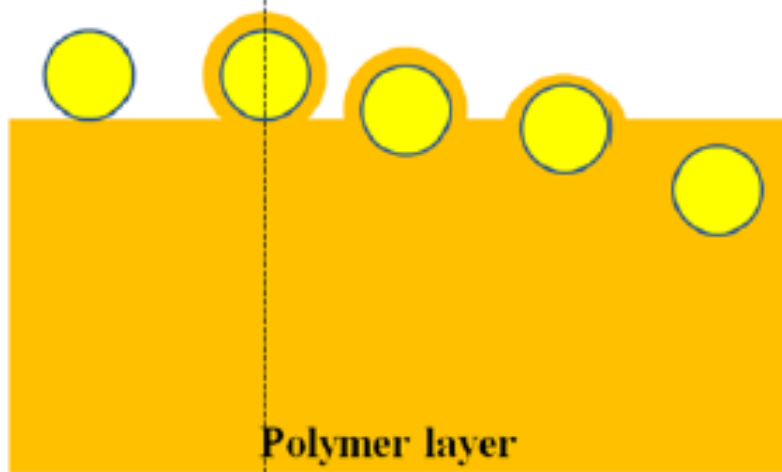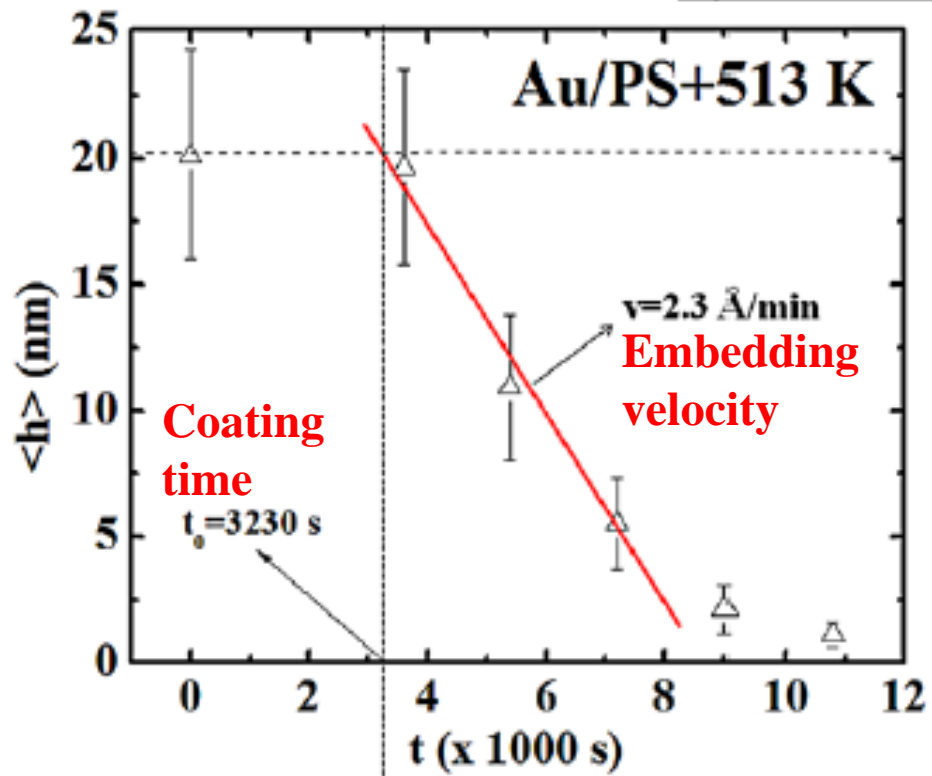
R. D. Deshmukh et al., Langmuir 23, 13169 (2007)

J. H.Teichroeb et al., Phys. Rev. Lett. 91, 016104 (2003)

V. Zaporojtchenko et al., Macromolecules 34, 1125 (2000)

R. Weber et al., Macromolecules 36, 9100 (2003)

J. Erichsen et al., Macromolecules 37, 1831 (2004)

- The driving force for the embedding process is given by the contribution of the metal clusters with radius h to the Gibbs free energy G, which is lowered upon embedding. The contribution of a single, spherical cluster is given by

$$G(L) = \pi\gamma_P L^2 - 2\pi h(\gamma_M - \gamma_{MP})L + \\ + 2\pi h^2\left(\gamma_{MP} + \gamma_M - 1/2\gamma_P\right)$$

L being the embedding depth from the surface to the center of the cluster.

- So, the surface Gibbs free energy can be reduced by embedding if the surface tension γ_M of the metal particles exceeds the sum of the interfacial tension γ_{MP} and the polymer surface tension
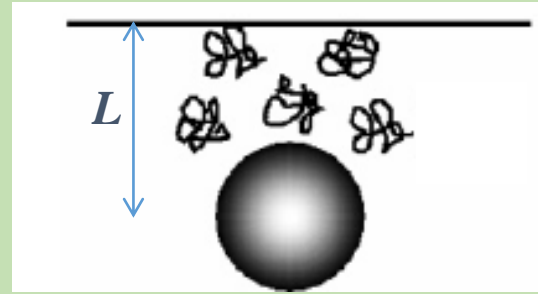
$$\gamma_M > \gamma_P + \gamma_{MP}$$

This relation is always fulfilled for metals on polymers, since the cohesive energy of polymers is so much lower than that of metals ($\gamma_P \ll \gamma_M$)

$\gamma_M \sim 1\text{-}2\ J/m^2$ $\gamma_P \sim 0.1\ J/m^2$

- The embedding of clusters of some nanometers should certainly require long-range chain mobility, which proceeds in experimentally accessible time scales above the glass transition.

G.J. Kovacs, P.S. Vincett, Thin Solid Films 111, 65 (1984)

C) Activation energy for the embedding process
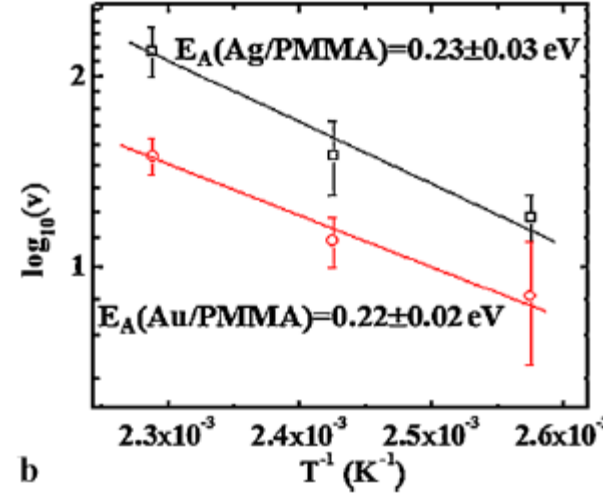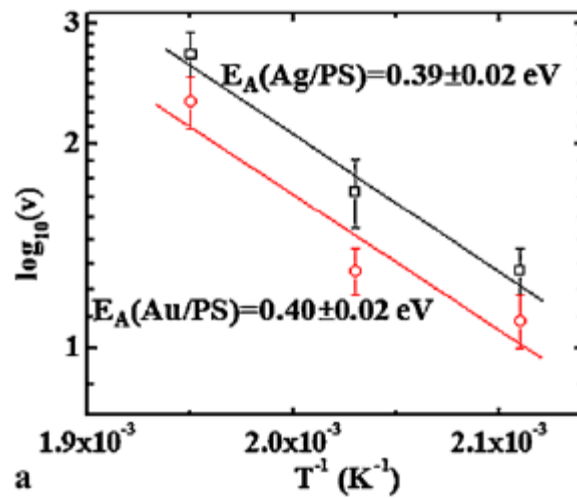
$$v = v_0 \exp[-E_A / kT]$$

E_A depends only on the polymer nature!

$E_A(Ag/PS)=0.39\pm0.02$ eV
$E_A(Au/PS)=0.40\pm0.02$ eV
$E_A(Ag/PMMA)=0.23\pm0.03$ eV
$E_A(Au/PMMA)=0.22\pm0.02$ eV

D) Embedding statistics: Weibull
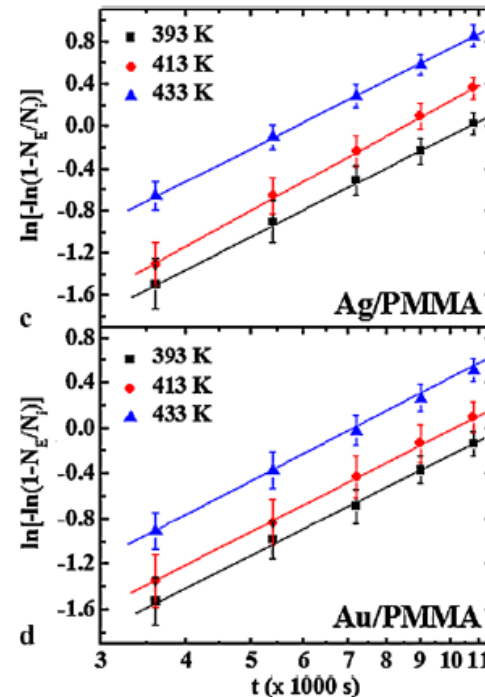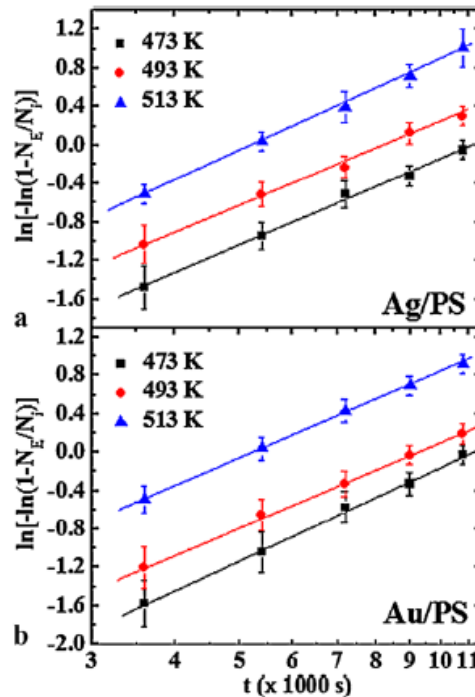
$$\frac{N_E}{N_0} = 1 - \exp\left[-\left(\frac{t}{\alpha}\right)^\beta\right]$$

α= scale factor (modal value of the distribution)= mean embedding time
β the shape parameter (Weibull slope)

	α (s)			β		
	393 K	413 K	433 K	393 K	413 K	433 K
Ag/PMMA	10,698	8562	5838	1.37	1.48	1.41
Au/PMMA	12,198	9984	7320	1.24	1.37	1.31

	α (s)			β		
	473 K	493 K	513 K	473 K	493 K	513 K
Ag/PS	10,938	8364	5268	1.32	1.23	1.31
Au/PS	10,962	9288	5244	1.41	1.28	1.31

E) General picture and methodology potentialities

A) In the polymer spin-coating stage we can tune d
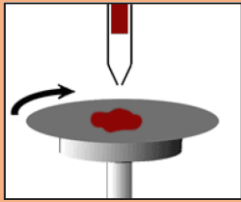
PMMA or PS

Si

PMMA or PS

Si

B) In the sputtering stage we can tune h_0 and N_0

PMMA or PS

Si

PMMA or PS

Si

C) In the annealing stage we can tune how many particles embedding

Si

Si

We can tune the metal volume fraction and so the physical properties of the system (conductivity, absorption,….)

Surface free energies considerations

a) in the initial growth stage noble metals grow as spherical clusters on polymer surfaces. In fact, the cohesive energy of metals is typically 2 orders of magnitude higher than the cohesive energy of polymers. Furthermore, the interaction between moderately reactive metals and polymers is generally very weak in comparison to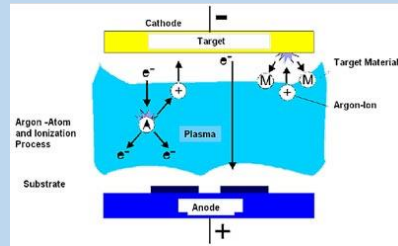 the strong metal–metal binding forces. Therefore, metals of low reactivity do not wet untreated polymer surfaces. They form clusters during the initial stage of polymer metalization. In our specific cases, the Au and Ag surface free energies are $\gamma_{Au} \sim$ 1500 mJ/m^2 and $\gamma_{Ag} \sim$ 900 mJ/m^2, respectively, while the PS and PMMA surface free energies are $\gamma_{PS} \sim$ 30−40 mJ/m^2 and $\gamma_{PMMA} \sim$ 30−40 mJ/m^2, respectively

$\gamma_{Au} \sim$ **1500 mJ/m^2**

$\gamma_{Ag} \sim$ **900 mJ/m^2**

$\gamma_{PS} \sim$ **30−40 mJ/m^2**

$\gamma_{PMMA} \sim$ **30−40 mJ/m^2**
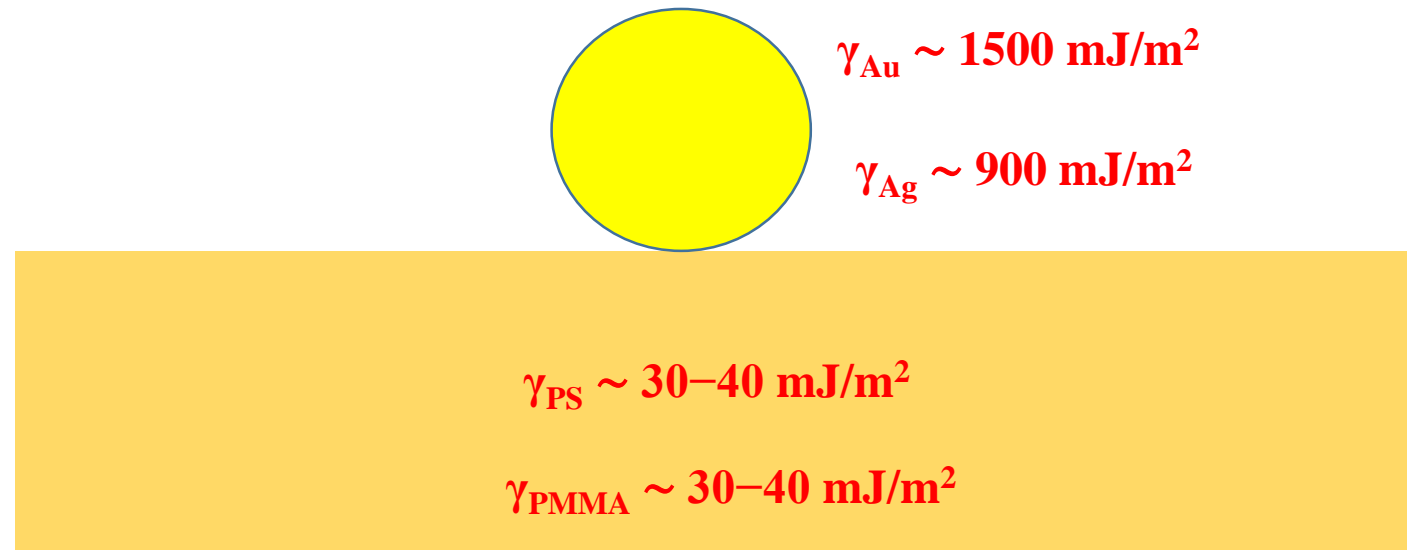
K. Tanaka et al., Macromolecules 29, 3040 (1996); C.E. Wilkes, J.W. Summers, C.D. Daniels (eds.), PVC Handbook (Hanser Gardner Publications, Cincinatti, 2005); I.C. Sanchez, Physics of Polymer Surfaces and Interfaces (Butterworth-Heinemann, Boston, 1992)

higher for PS than that PMMA. Analyzing further the embedding velocities of the NPs, we can observe that, for each fixed T, v is higher for the Ag/PS system, a little bit lower for the Au/PS system, a further little bit lower for the Ag/PMMA system, and, finally, lower for the Au/PMMA system: $v_{Ag/PS} > v_{Au/PS} > v_{Ag/PMMA} > v_{Au/PMMA}$. An explanation of such a behavior can be found considering the interaction between the metal atoms and the polymer chains on the basis of van der Waals forces which provide a long-range interaction [24]. The material-dependent Hamaker constants A serve as a measure of the strength due to dispersion forces. The relevant values in our cases are: the interaction between the PS chains, quantified by the Hamaker constant $A_{PS,PS} = 6.2 \times 10^{-20}$ J [24–26, 38]; the interaction between the PMMA chains, quantified by the Hamaker constant $A_{PMMA,PMMA} = 7.1 \times 10^{-20}$ J [39, 40]; the interaction between the Au atoms, quantified by the Hamaker constant $A_{Au,Au} = 41.2 \times 10^{-20}$ J [24–26, 38]; the interaction between the Ag atoms, quantified by the Hamaker constant $A_{Ag,Ag} = 39.1 \times 10^{-20}$ J [39, 40]. From these values, we can estimate the interaction between the Ag atoms and the PS chains, quantified by the Hamaker constant $A_{Ag,PS} = \sqrt{A_{Ag,Ag} \times A_{PS,PS}} = 15.6 \times 10^{-20}$ J; the interaction between the Ag atoms and the PMMA

PS chain   PS chain

$A_{PMMA,PMMA} = 6.2 \times 10^{-20}$ J

PMMA chain   PMMA chain

$A_{PMMA,PMMA} = 7.1 \times 10^{-20}$ J

Au atom   Au atom

$A_{Au,Au} = 41.1 \times 10^{-20}$ J

Ag atom   Ag atom

$A_{Ag,Ag} = 39.1 \times 10^{-20}$ J
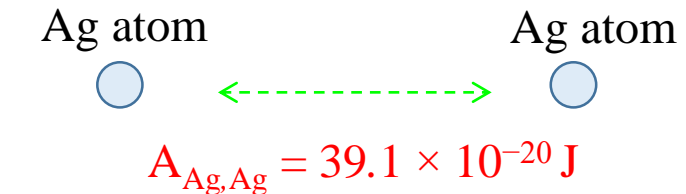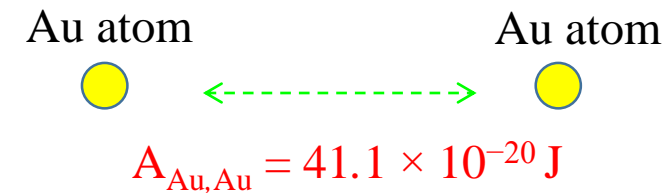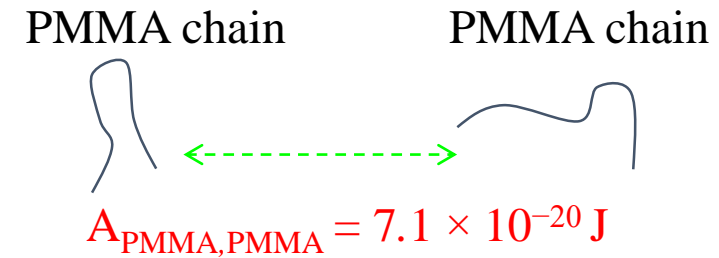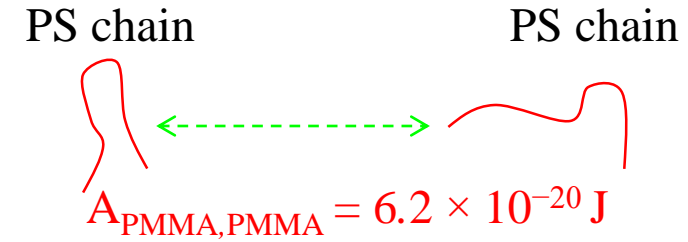
chains, quantified by the Hamaker constant $A_{Ag,PMMA} = \sqrt{A_{Ag,Ag} \times A_{PMMA,PMMA}} = 16.6 \times 10^{-20}$ J; the interaction between the Au atoms and the PS chains, quantified by the Hamaker constant $A_{Au,PS} = \sqrt{A_{Au,Au} \times A_{PS,PS}} = 16.0 \times 10^{-20}$ J; the interaction between the Au atoms and the PMMA chains, quantified by the Hamaker constant $A_{Au,PMMA} = \sqrt{A_{Au,Au} \times A_{PMMA,PMMA}} = 17.1 \times 10^{-20}$ J. On the basis of these calculations we have $A_{Ag/PS} < A_{Au/PS} < A_{Ag/PMMA} < A_{Au/PMMA}$. Now, we can, also, consider that the viscosity η of the NPs in the polymer, during the embedding process, is directly proportional to the relative Hamaker constant interaction. For example, on the basis of the Kovac and Vincett model [19, 20]

$$\eta = \frac{A_{M,P} t}{h^3 4\pi} \left(\frac{4}{3} x^3 + x^4 + \frac{1}{5} x^5 \right)^{-1} \tag{5}$$

$A_{M,P}$ being the metal–polymer Hamaker constant, t the embedding time, h the NPs radius, $x = z/h$ with z the embedding depth. Therefore, as $\eta \propto A_{M,P}$, and in our case, $A_{Ag/PS} < A_{Au/PS} < A_{Ag/PMMA} < A_{Au/PMMA}$, we can deduce, with parity of other conditions, that $\eta_{Ag/PS} < \eta_{Au/PS} < \eta_{Ag/PMMA} < \eta_{Au/PMMA}$. Finally, since $v \propto 1/\eta$ we can, also, deduce that $v_{Ag/PS} > v_{Au/PS} > v_{Ag/PMMA} > v_{Au/PMMA}$, as we observed by the experimental data.

$$\eta \propto A_{MP}$$
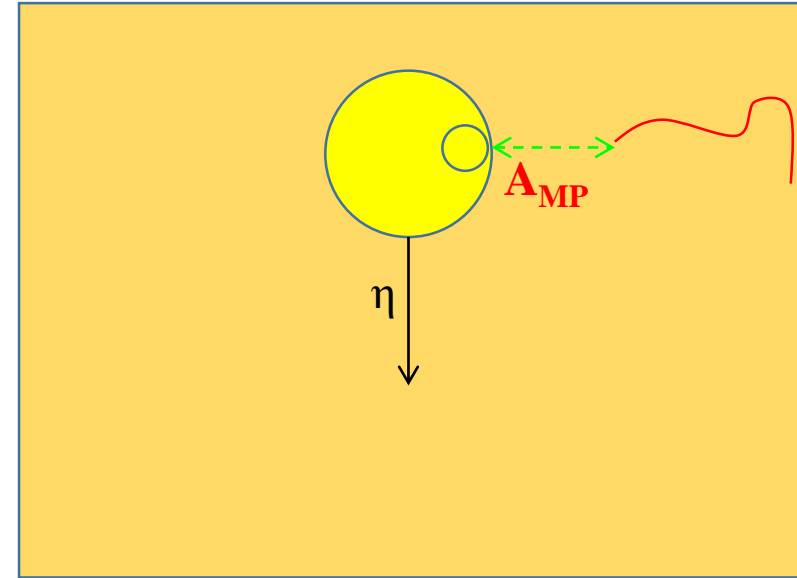
$$v \propto 1/A_{MP}$$

$A_{Ag,PS} = 15.6 \times 10^{-20}$ J	$v_{Ag,PS}$
$\wedge$	$\vee$
$A_{Au,PS} = 16.0 \times 10^{-20}$ J	$v_{Au,PS}$
$\wedge$	$\vee$
$A_{Ag,PMMA} = 16.6 \times 10^{-20}$ J	$v_{Ag,PMMA}$
$\wedge$	$\vee$
$A_{Au,PMMA} = 17.1 \times 10^{-20}$ J	$v_{Au,PMMA}$

Shadowed depositions
(Glancing Angle Depositions)

Physical self-assembly and the nucleation of three-dimensional nanostructures by oblique angle deposition

T. Karabacak,[a] G.-C. Wang, and T.-M. Lu
Department of Physics, Applied Physics and Astronomy, Rensselaer Polytechnic Institute, Troy, New York 12180-3590
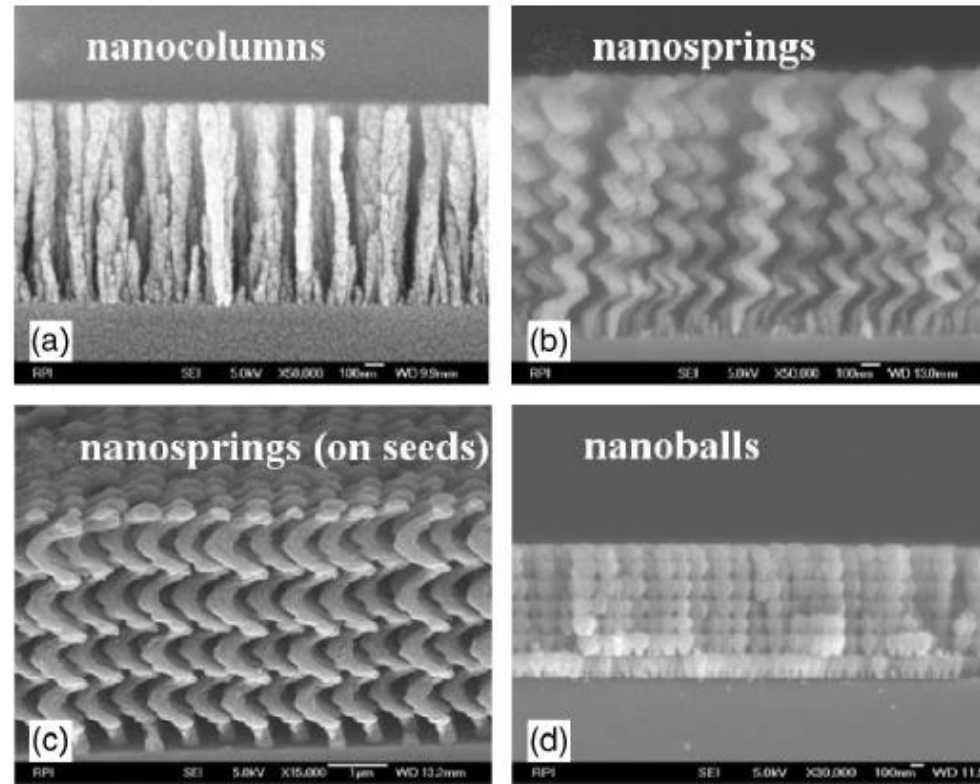
FIG. 1. SEM cross-section images of some nanostructures obtained by oblique angle deposition. All nanostructures are made of silicon.

Advanced techniques for glancing angle deposition

K. Robbie,[a] J. C. Sit, and M. J. Brett
*Department of Electrical and Computer Engineering, University of Alberta, Edmonton,
Alberta T6G 2G7, Canada*

When a thin film is deposited by physical vapor deposition, with the vapor flux arriving at an oblique angle from the substrate normal, and under conditions of sufficiently limited adatom mobility to create a columnar microstructure, the resulting structure is somewhat porous and grows at an angle inclined toward the vapor source. For a given material and set of deposition conditions, there is a fixed relationship between the angle of vapor flux incident on the substrate and the inclination angle at which the columnar thin film grows. As the porosity of the film is also dependent on the incident flux angle, column growth angle and porosity cannot be chosen independently. If a large columnar angle (more parallel to the substrate) is desired, the flux must be deposited at a large oblique angle resulting in a very porous film. Conversely, if a near vertical columnar film is desired, the flux must arrive more perpendicular to the substrate and the resulting film has a tightly packed, dense microstructure. We present a technique, based on glancing angle deposition, employing substrate motion during deposition, which allows the columnar growth inclination angle and film density to be controlled independently. With this method, microstructurally controlled materials can be fabricated with three dimensional control on a 10 nm scale for use in optical, chemical, biological, mechanical, magnetic, and electrical applications. © *1998 American Vacuum Society.* [S0734-211X(98)10803-X]
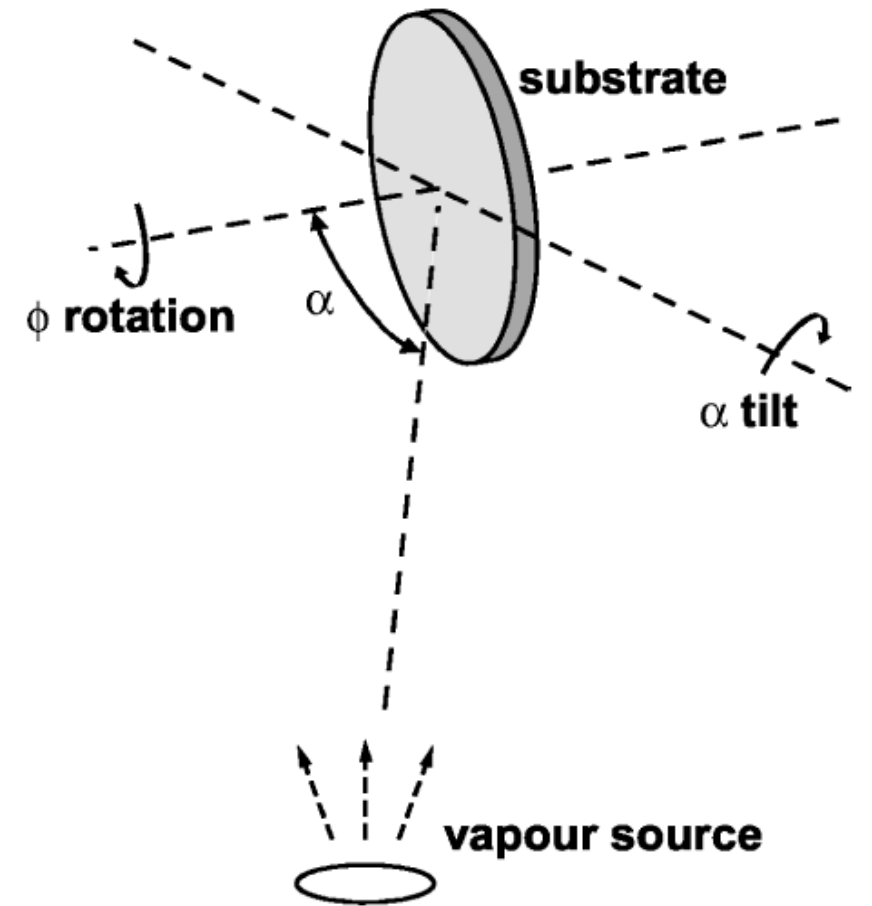
FIG. 1. Schematic of the GLAD process. The step motor that rotates the substrate (ϕ rotation) has a 0.9° resolution. The step motor that sets the flux angle α has a 0.18° resolution.
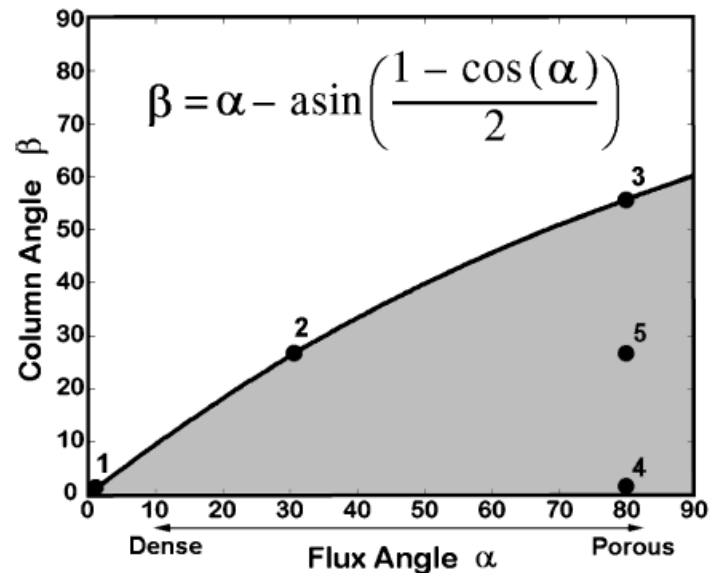
FIG. 3. Solid line is the relationship given by Tait (Ref. 13) and describes the fixed relationship between the incident flux angle α and the columnar growth angle β for a fixed set of deposition conditions (material, temperature, gas composition and pressure, and vapor energetics). The shaded region is the microstructure attainable with the technique described in this work.

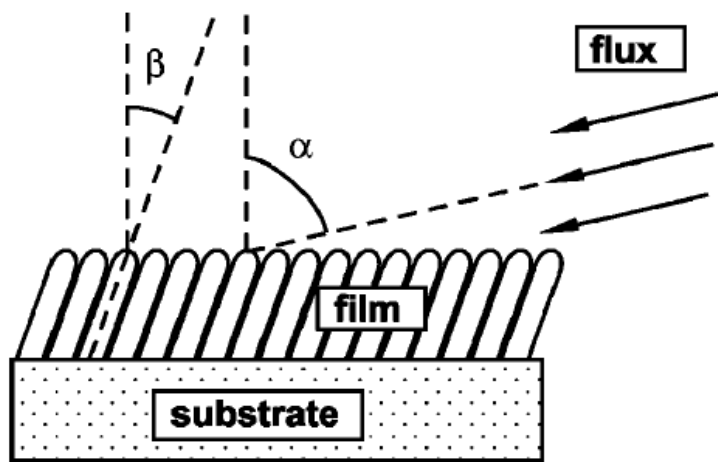$$\beta = \alpha - \text{asin}\left(\frac{1 - \cos(\alpha)}{2}\right)$$

FIG. 2. Schematic of deposition vapor flux and film orientation with angle definitions. α is the flux arrival angle measured from the substrate normal and β is the columnar microstructure inclination angle also measured from the substrate normal.
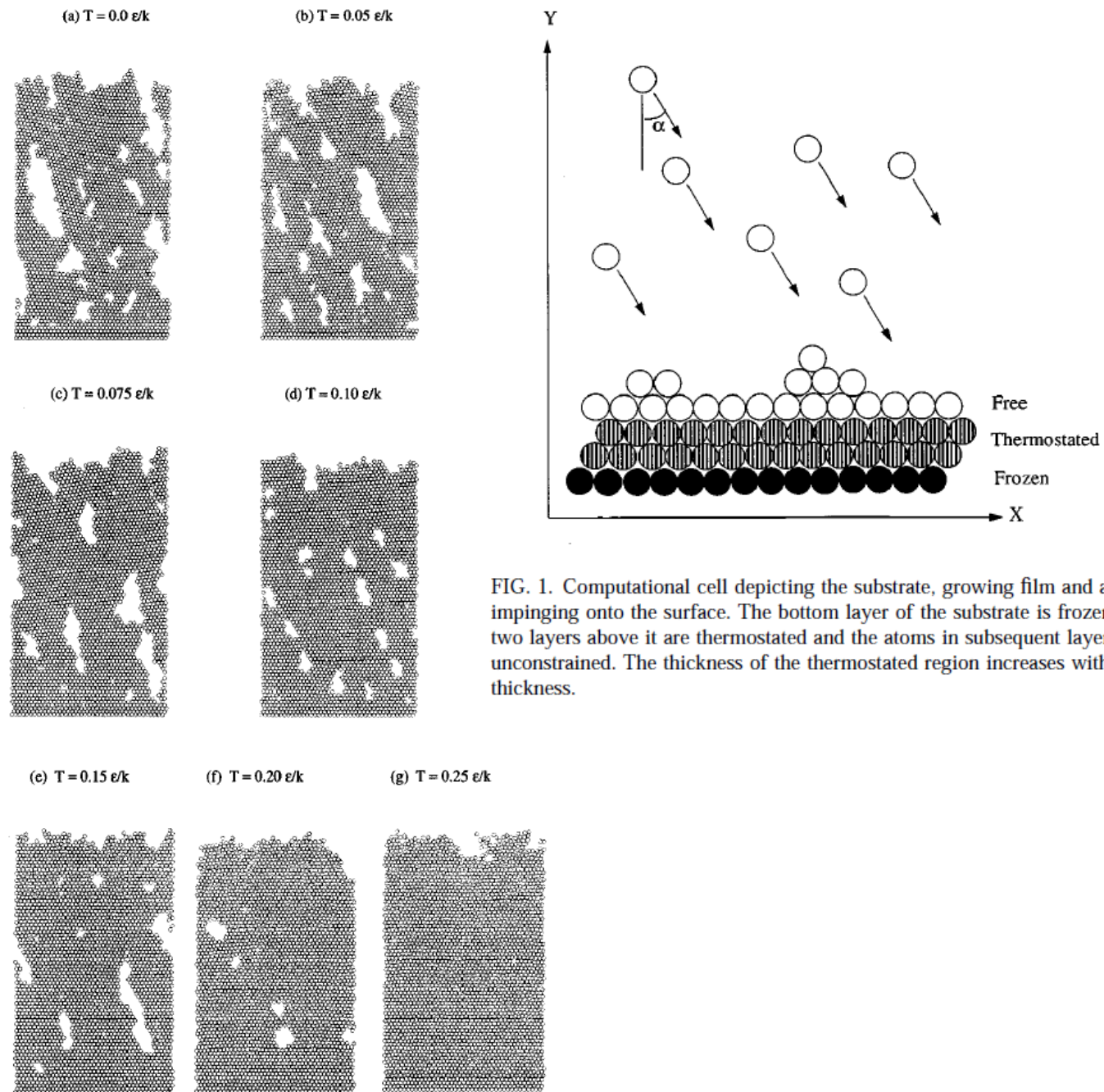
FIG. 1. Computational cell depicting the substrate, growing film and atoms impinging onto the surface. The bottom layer of the substrate is frozen, the two layers above it are thermostated and the atoms in subsequent layers are unconstrained. The thickness of the thermostated region increases with film thickness.

(a) T = 0.0 ε/k   (b) T = 0.05 ε/k

(c) T = 0.075 ε/k   (d) T = 0.10 ε/k

(e) T = 0.15 ε/k   (f) T = 0.20 ε/k   (g) T = 0.25 ε/k

FIG. 2. Typical microstructures of films grown at various substrate temperatures with fixed deposition rate, $E_b = 0.80\ \epsilon$ and $\alpha = 45°$.

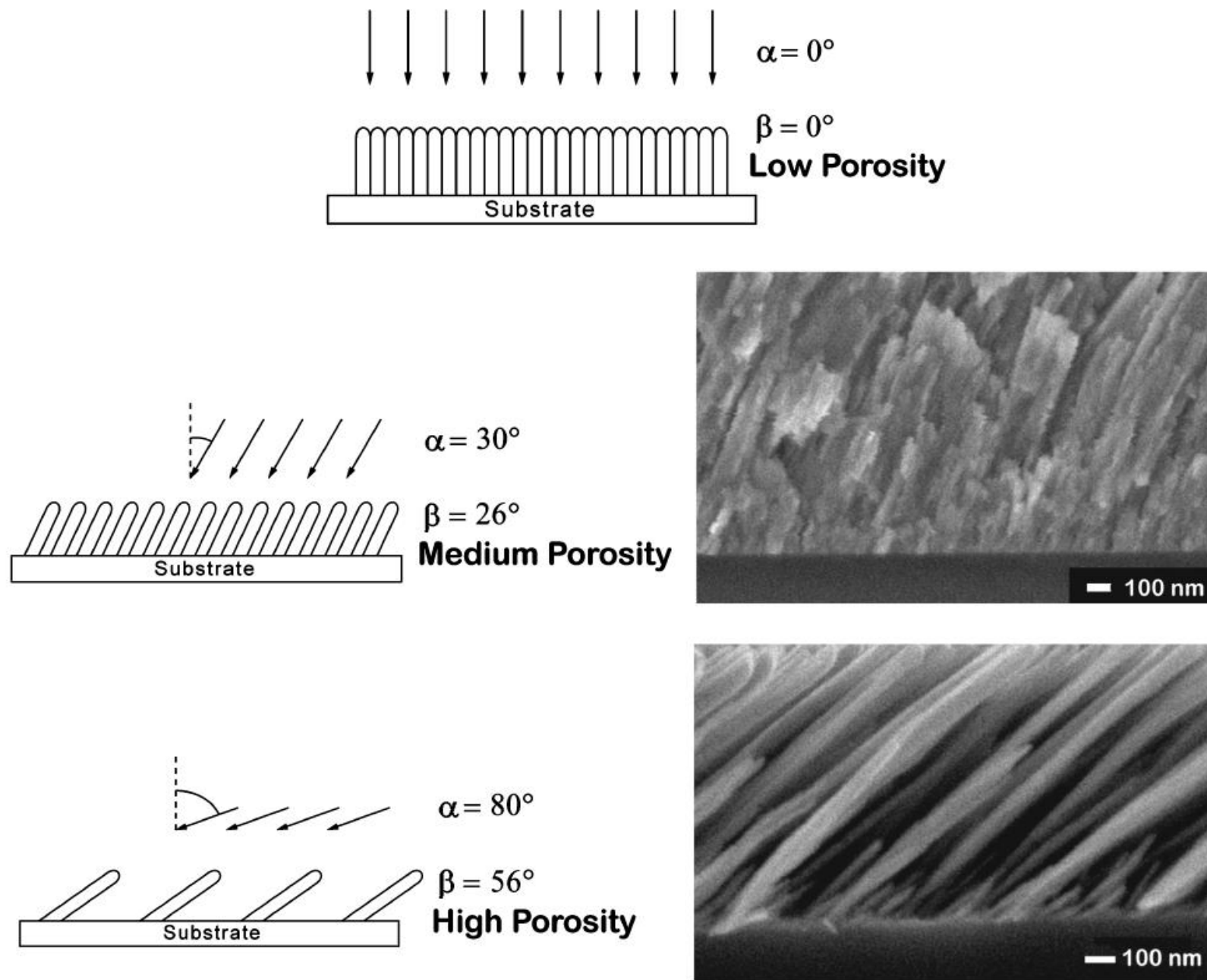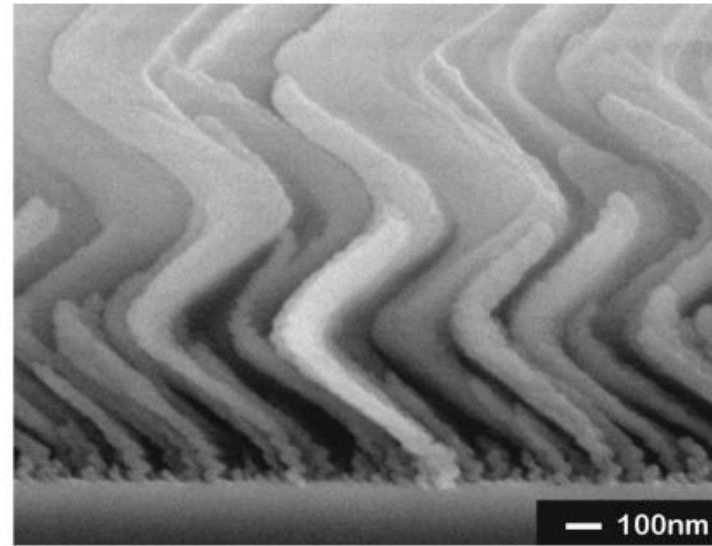FIG. 4. Cr films deposited at increasing oblique flux angle α onto stationary substrates. The film column angles β increase with flux angle in a relationship similar to that described by Tait (Ref. 13). The film porosity also increases with increasingly oblique flux angle.
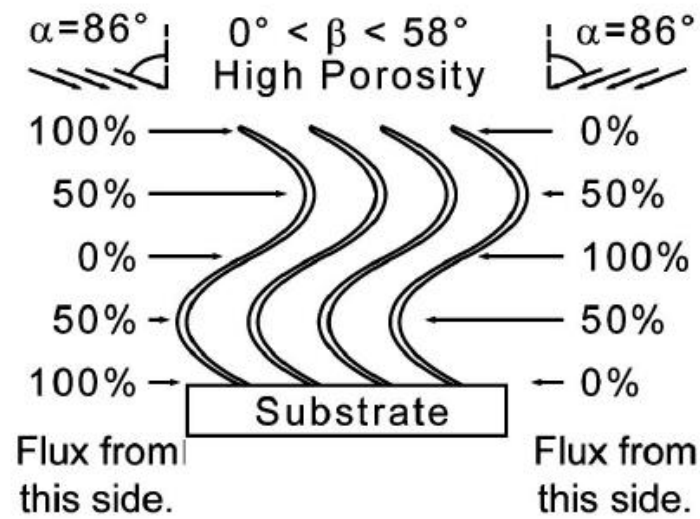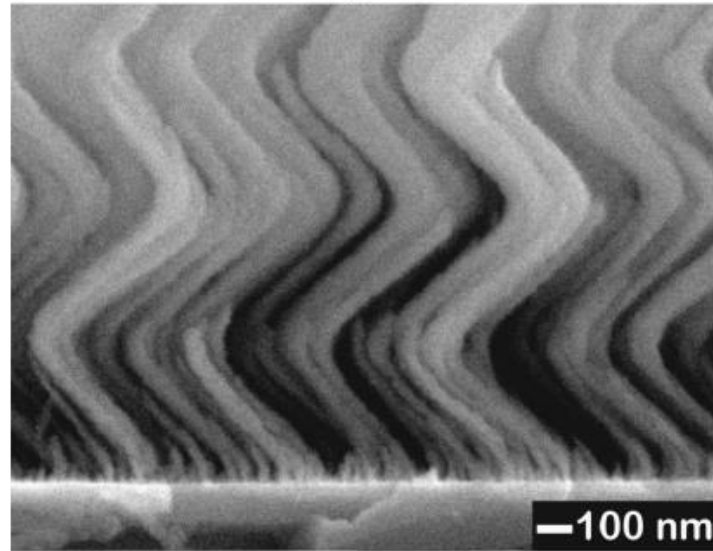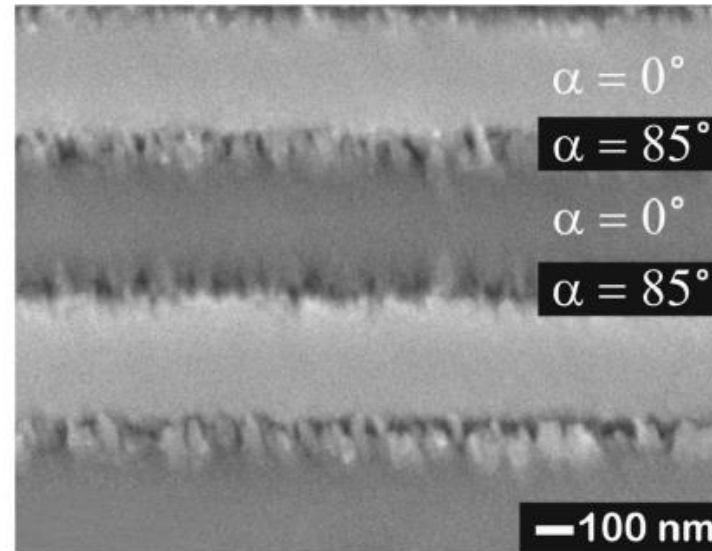
FIG. 7. Schematic description (a) and SEMs of SiO films with column inclination angle β varied dynamically during deposition while keeping the porosity constant (b) and (c). The flux angle α was fixed at 86° for (b) and (c). These are thin film realizations of constant density periodically bent nematics. In (d), the flux angle α was varied continuously between 0° and 85° four times with the substrate azimuthal position ϕ held constant.
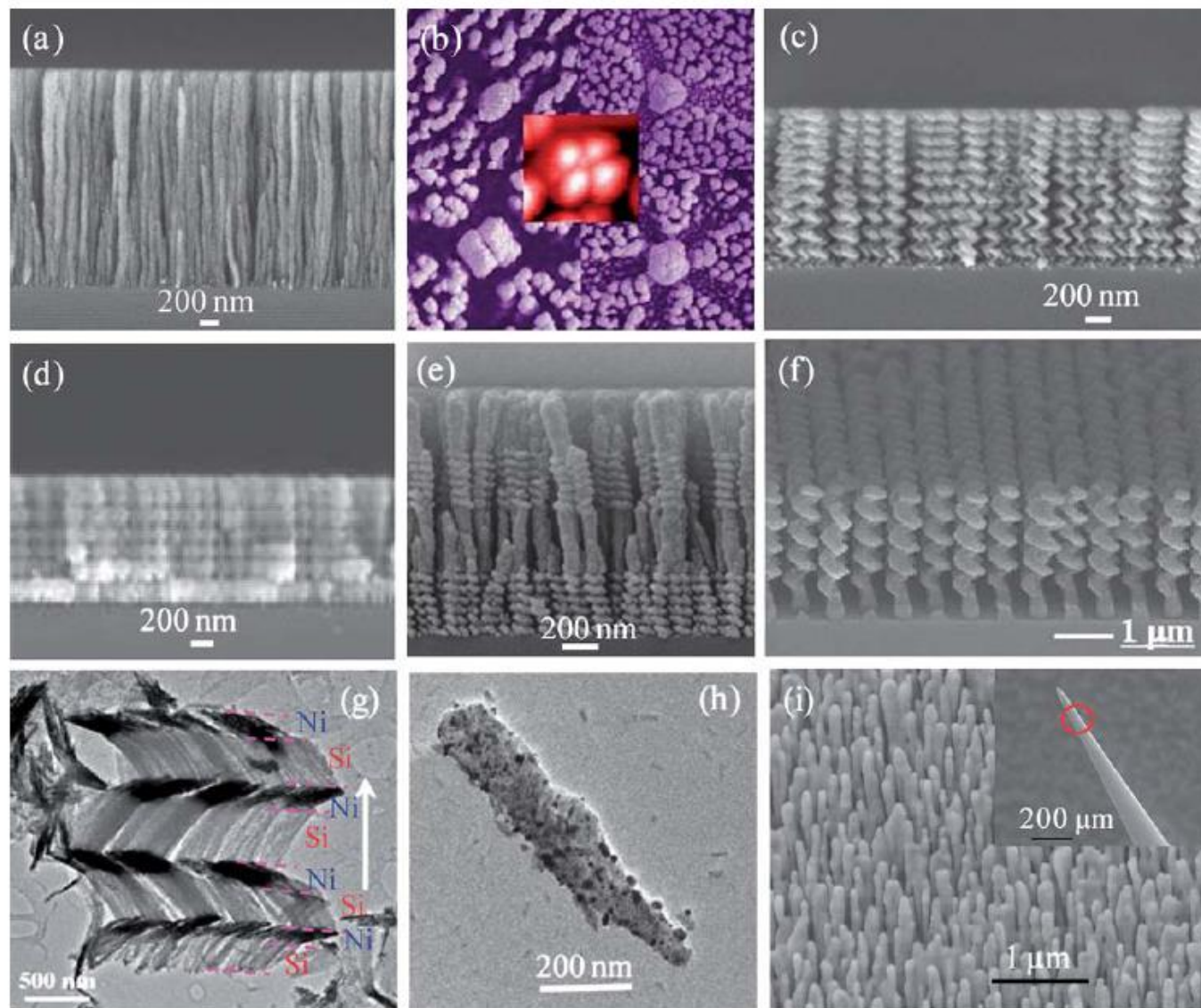
Fig. 2 Examples of electron micrographs of typical nanorods prepared by DSG/GLAD: (a) a vertically aligned Si nanorod array;[59] (b) nanorods with different shapes;[12] (c) a Si nanospring array;[59] (d) a bead-like multilayer Si array; (e) a multilayer array of nanosprings and nanorods;[22] (f) a regular array of Si nanosprings grown on W-plugs;[59] (g) a bundle of Si/Ni multilayer nanosprings;[49] (h) Ag nanoparticle decorated MgF$_2$ nanorod;[29] and (i) a Ag nanorod array deposited onto a tapered fiber where the inset shows the tapered fiber.[61] Reproduced from ref. 12 with permission of the American Chemical Society. Reproduced from ref. 22 with permission of the World Scientific Publishing. Reproduced from ref. 29 and 49 with permission of the WILEY-VCH. Reproduced from ref. 59 with permission of the Springer. Reproduced from ref. 61 with permission of the American Vacuum Society.

II. COLUMN FORMATION

A. Nucleation and initial growth

Thin film deposition involves a material undergoing a phase transition from a vapor above the substrate to a solid on the substrate.[7] The transition proceeds by the formation and growth of regions of the condensed material. This process, known as nucleation, is an important step in film growth as it influences many of the features observed in the final film microstructure.

The condensation of the vapor flux onto the surface is a complicated atomistic phenomenon.[8–10] The vapor provides a constant flux of incident atoms to the surface which, once adsorbed, will randomly diffuse across the substrate surface. The adsorbed atoms, or adatoms, will diffuse until they are consumed by one of a variety of microscopic process: two adatoms can join together forming a nucleus, single adatoms can attach to existing nuclei, or the adatom can reevaporate from the surface. Adatoms constituting a given nucleus may also diffuse along the nuclear boundary or detach from the nucleus altogether. Each of these individual processes occurs over a range of characteristic time scales, meaning that the importance of each process is governed by its respective energetics and kinetics. For example, once the nucleus reaches a critical size, energy considerations severely reduce the rate of adatom detachment from the nucleus. This critical size depends strongly on the characteristics of the system and may be as small as two joined adatoms.

Continued deposition will follow one of three growth regimes, depending on the surface and interfacial energetics of the substrate and condensing atoms.[11,12] When the atoms are more strongly bound to the substrate than to each other, growth will occur by monolayer formation. The nuclei which form in this regime are two dimensional and only a single atom in height. This growth mode is called layer or Frank–van der Merwe growth. The second type of growth occurs when the interaction between the atoms is greater than the interaction with the substrate, resulting in the formation of three-dimensional nuclei. This type of growth is called island or Volmer-Weber growth. The third growth regime is a combination of the previous two modes. Atoms will initially cover the surface in monolayers due to the strong interaction with the substrate, but after the deposition of one or several layers, islanding will occur. This growth mode is called layer plus island or Stranski-Krastanov growth.

The Volmer-Weber growth mode is the most important case for GLAD. This mode causes the formation of microscopic topologies which, at oblique angles of incidence, lead to ballistic shadowing. As the surface coverage increases, the nuclei will intercept greater and greater amounts of vapor flux. It is important to note that vapor condensation is a stochastic process and not all the nuclei which form will be identical. Arbitrary fluctuations in the local deposition rate combined with the random nature of adatom diffusion will lead to a variation in the size of nuclei. In addition, nucleation is enhanced at defects on the substrate (such as impurities, point defects, and edge defects), which will further increase this diversity.[13] This is a meaningful consideration, as it randomizes the surface distribution of columns in later stages of film growth.

B. Column formation and film microstructure: Structure zone models

Progressing beyond the intial stage of nucleation, film growth continues as vapor species deposit onto the film surface. Surface diffusion is still an important factor, and the bulk diffusion of atoms within the film also begins to impact the growth. In addition to the incident energy of the particles, energy for atomic diffusion is acquired as thermal energy from the environment. The substrate temperature T_s has, therefore, always been recognized as a major determinant of thin film structure.
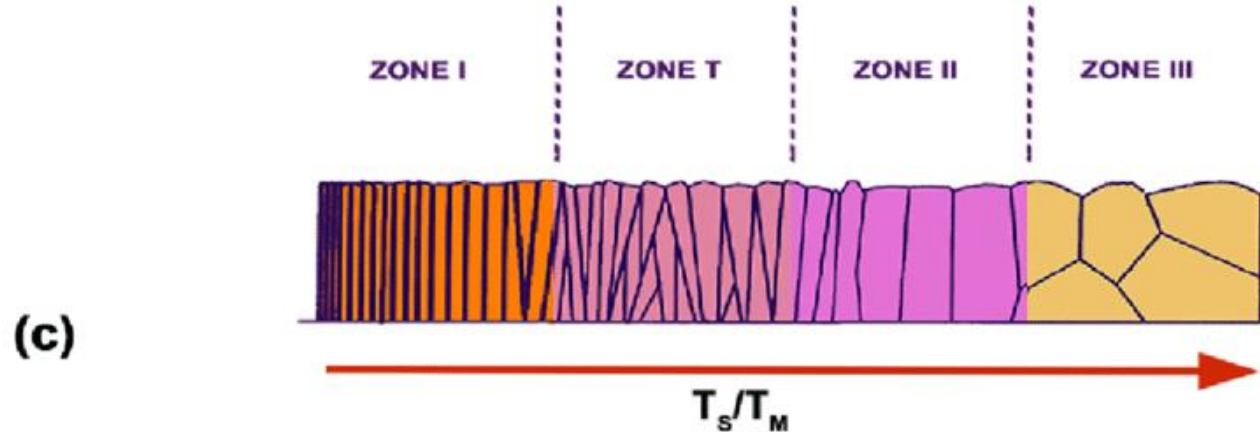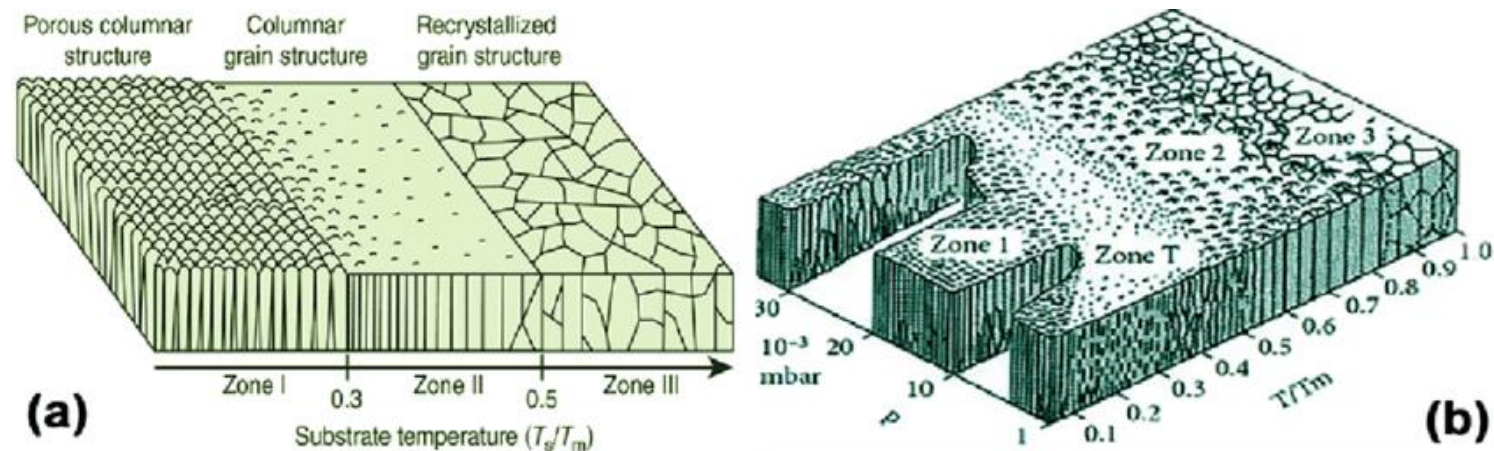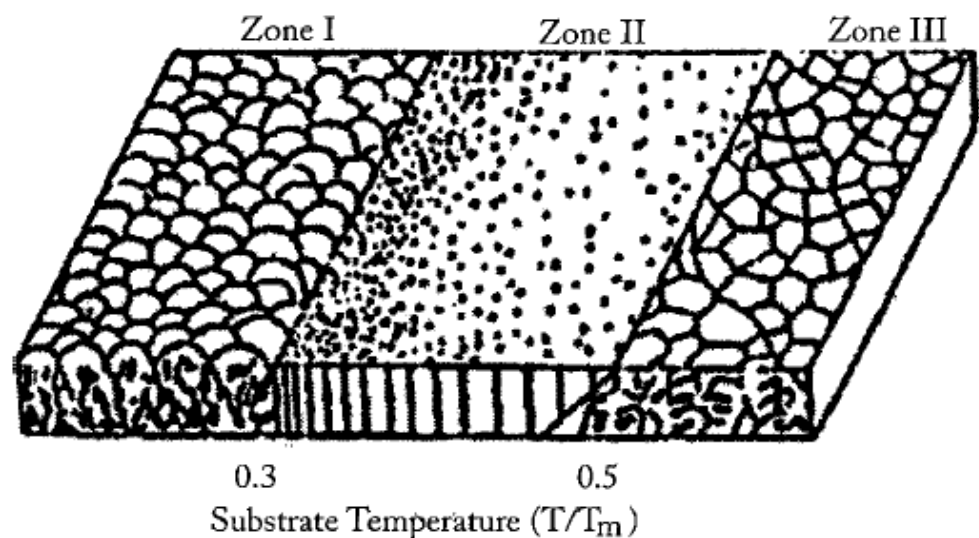
FIG. 3. Structure zone model of Movchan and Demchishin is succinctly presented by plotting the observed microstructure over a range of temperatures (normalized to the melting point of the material). The transition temperatures between zones I and II and between zones II and III occur at 0.3 and 0.5, respectively. Image adapted from (Ref. 14).

Early experiments by Movchan and Demchishin[14] led to an understanding of how substrate temperature affects film growth. They proposed a three region structure zone model (SZM) that provides an overview of their findings. In these studies, thermal gradients were maintained across substrates during deposition at normal incidence, and the microstructure of the films was examined. As the substrate temperature was increased, they were able to identify three distinct structural zones (labeled zones I, II, and III) with transitions occurring at temperatures T_1 and T_2, where the ratio of T_1 and T_2 to the melting point T_m was remarkably consistent from material to material ($T_1/T_m \approx 0.3$ and $T_2/T_m \approx 0.5$). In the first zone ($T_s < T_1$), the temperature is too low for any significant diffusion to occur. The film microstructure is composed of tapered columns with domed tops and the columns are separated by voids. Increasing the temperature leads to a gradual increase in the column diameter, until the substrate temperature reaches T_1. In this second zone ($T_1 < T_s < T_2$), the tapering disappears leading to a denser and more clearly defined columnar structure. The column diameter increases as the temperature is increased, although the overall structure is maintained. Due to the increased substrate temperature, surface diffusion strongly influences the growth. At the second transition temperature ($T_2 < T_s$), the third zone is entered and there is sufficient energy for bulk diffusion to occur, leading to recrystallization as the film grows. In this zone, the structure consists of equiaxed grains whose size increases with increasing temperature. The characteristic structure of each zone in this model, as well as the transition temperature, is shown in Fig. 3. GLAD principally relies on characteristics of growth in the first zone of this model, where limited surface diffusion leads to the formation of columnar grains.
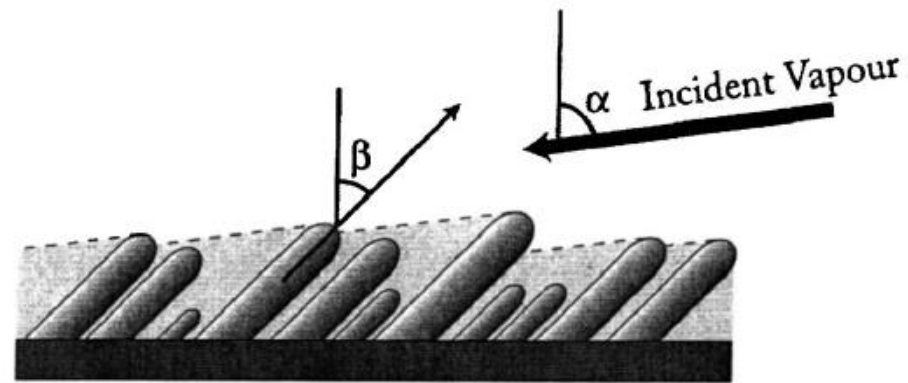

FIG. 6. Columns will grow oriented toward the source, forming an angle β with the substrate normal ($\beta < \alpha$).

Parameter	Reference	Material	PVD Method	α (deg)
Interface width	33	SiO$_2$	Electron beam evaporation	87
		Ti	Electron beam evaporation	87
Interface width	34	Cr	Magnetron sputtering	89
Intercolumn spacing	35	Si	Electron beam evaporation	87
Intercolumn spacing	36	Ru	Magnetron sputtering	85
Column diameter	37	Si	Electron beam evaporation	75
				83
				85
				87
				89
Column diameter	38 and 39	Si	Thermal evaporation	85
		Cu	Thermal evaporation	85
		Co	Thermal evaporation	85
		W	Magnetron sputtering	87
Column diameter	40	Si	Thermal evaporation	85
Column diameter	35	Si	Electron beam evaporation	87

The diffusion will be governed by Fick's law, moving adatoms from the columns tips (where adatom concentration is highest) toward the shadowed areas (where adatom concentration is lowest). Surface diffusion therefore counteracts the effects of shadowing, allowing adsorbed adatoms to diffuse into the shadowed region. Surface diffusion can be considered to be a thermally activated Arrhenius-type process where the diffusion coefficient D is proportional to

$$D \propto \exp(- E_a/k_b T_s), \tag{6}$$

where T_s is the substrate temperature, k_b is Boltzmann's constant, and E_a is the energy barrier of the diffusion process. The adatoms acquire thermal energy from the surface in order to overcome this energy barrier, which depends on the adatom and substrate material. The displacement r of the adatoms over the substrate surface is given by the relation

$$\langle r \rangle = \sqrt{2D\tau}, \tag{7}$$

where $\langle \ \rangle$ represents a statistical averaging and τ is the diffusion time. An elevated temperature leads to an increased diffusion coefficient and the adatoms will be able to diffuse a greater distance. The diffusion time is determined by one of two rate-limiting factors; the adatom will diffuse on the surface until it either evaporates from the surface or it is buried by the arrival of new atoms. In the case of GLAD, the latter event is more significant.
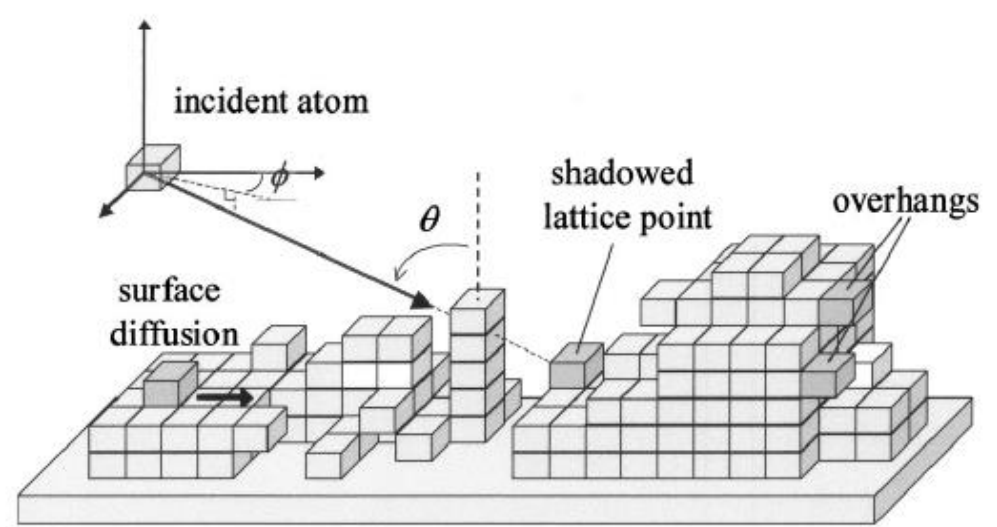

FIG. 5. A schematic of the three-dimensional Monte Carlo simulations for oblique angle deposition.
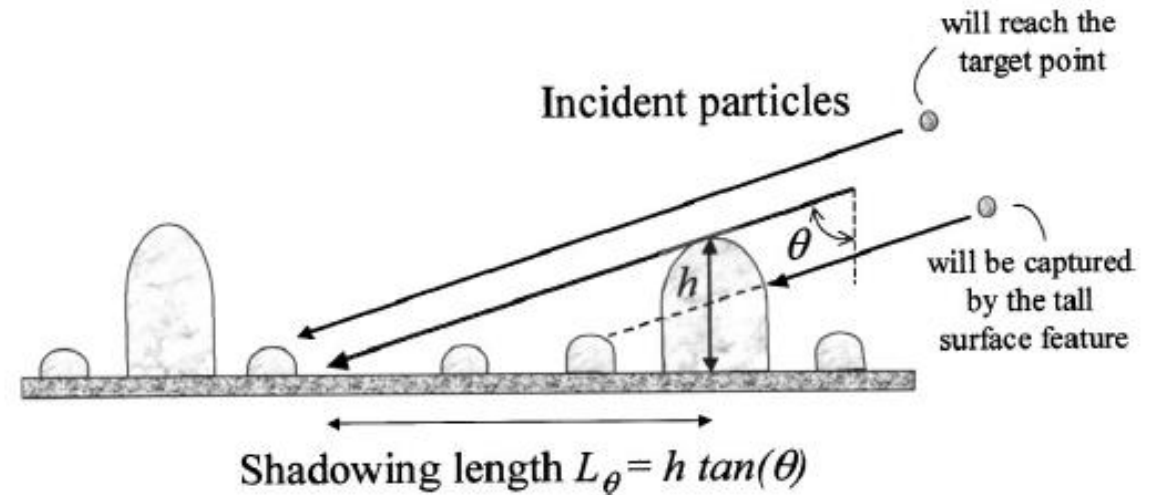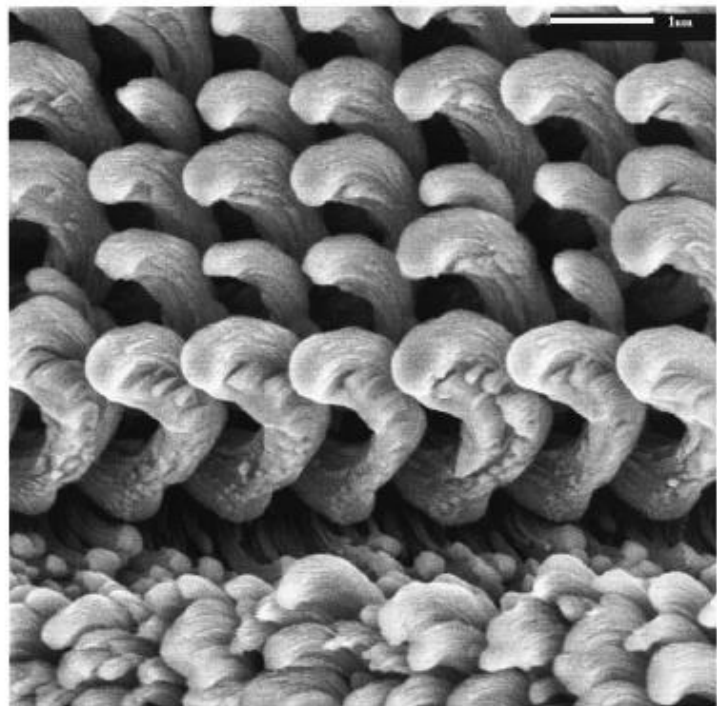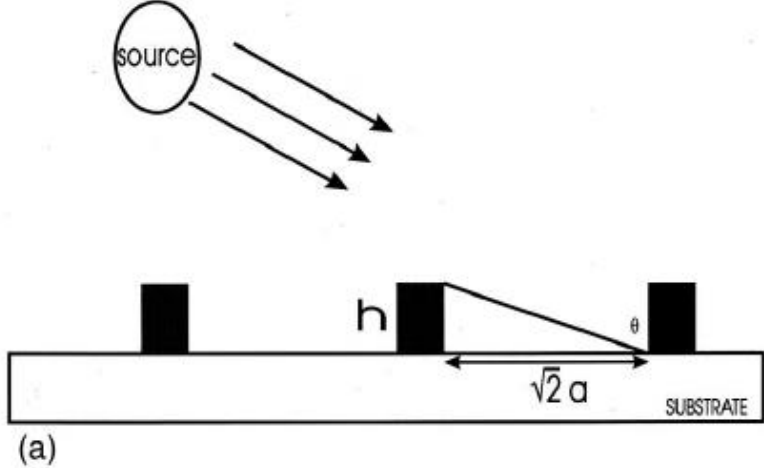

FIG. 9. A schematic that shows the definition of shadowing length L_θ.
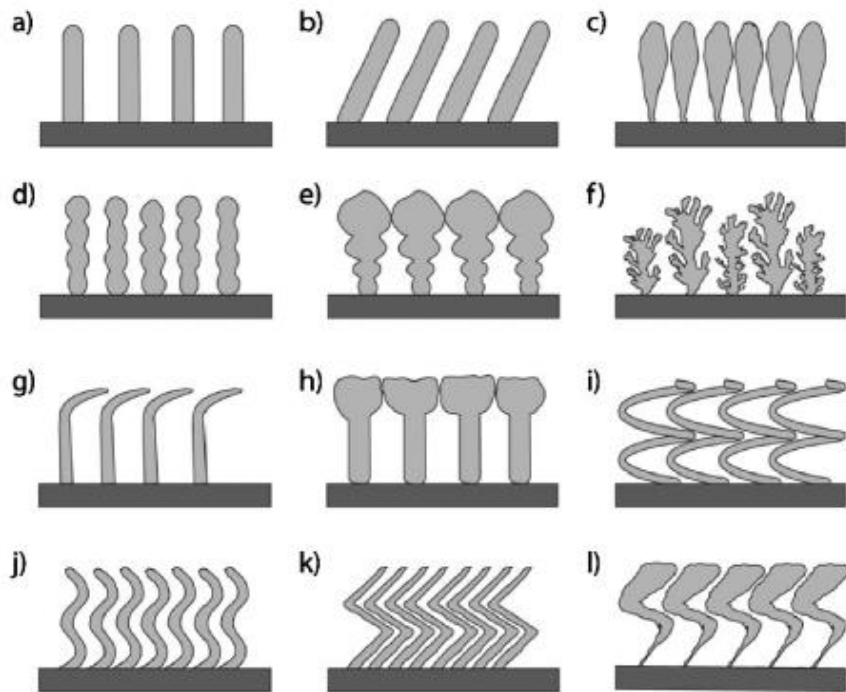
(a)

(b)

FIG. 1. Schematic depiction of various nanostructures obtained in GLAD thin films: (a) straight pillars, (b) inclined columns, (c), (d), (e) pillars with variable diameter, (f) fractal-like structures, (g), (h) columns with capping layers, (i) helix, (j) waved columns, (k) zig–zag, (l) zig–zag pillars with varying diameter.

The basic requirements for glancing angle deposition of high quality thin films with controlled nanostructure are the following:

(1) Control of substrate rotation and tilt orientation relative to the vapor source to allow synthesis of thin films with specific nanostructure. In addition, there is a clear requirement for good control over all deposition conditions that affect the microstructure of deposited thin films.

(2) A highly collimated or point-like vapor source that can provide a narrow angular distribution of flux arriving on the substrate. As geometrical shadowing is critical to the GLAD technique, directionality in the arriving vapor is necessary. A small source such as an evaporator or an effusion cell is best, and background gas pressure must be reduced to minimize gas scattering of the vapor.

(3) Variable substrate temperature in order to enable variation of film nanostructure by controlling heat input to the nucleation and aggregation processes.

(4) Synthesis of thin films in a controlled environment. The deposition has to be performed at a vacuum better than 10^{-6} Pa (10^{-8} Torr) in order to minimize the effects of thin films contamination.

(5) The existence of a fast and easy transfer mechanism of specimens from atmospheric conditions to an UHV environment at a specific sample orientation. An efficient UHV chamber design allows the introduction and removal of samples or substrates without venting and pumping the main chamber, saving considerable time.

(6) The load-lock chamber has to be equipped with several sample holders to make the introduction and removal of specimens efficient.

(7) The deposition parameters must be controlled by computer and all process parameters must be monitored throughout the deposition process.
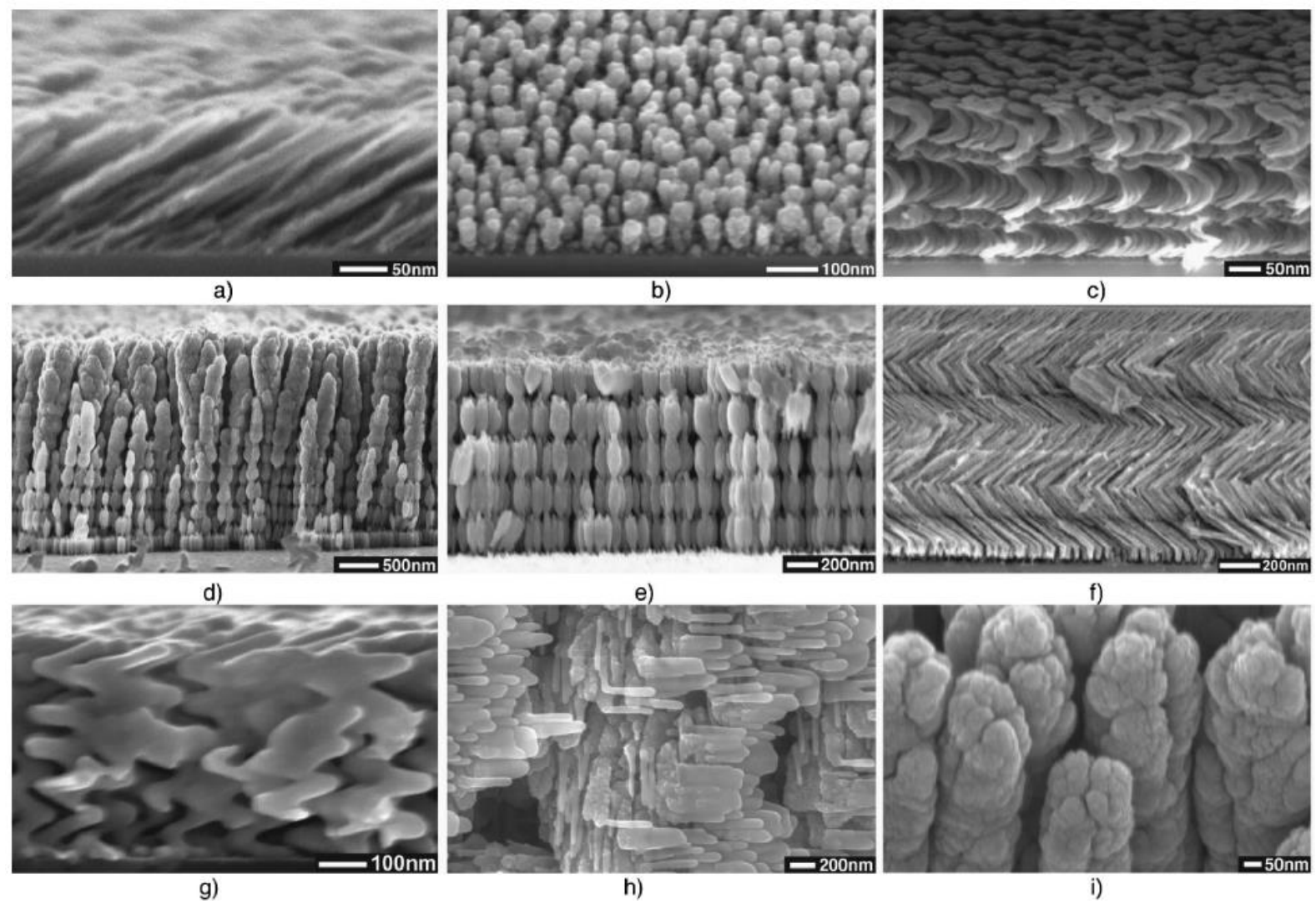
We have successfully deposited Ag, Al, Au, Cu, Co, Cr, Ni, Si, Ti, Mo, MgF$_2$, SiO$_2$, on substrates of glass, Si, SiC, and SiO$_2$. Depositions of films of different thickness have been carried out at constant rates of 0.2–0.5 nm/s onto substrates with various orientation and rotation programs.

IV. FILM PROPERTIES AND TECHNOLOGICAL APPLICATIONS

Microstructured thin films fabricated using GLAD have found application in diverse fields, capitalizing on the unique physical properties of the films. There are two main advantages inherent to GLAD films. First, because the films possess an internal microstructure, the exposed surface area of the film is dramatically higher than in a dense coating. Second, the particular geometry of the micro- and nanostructures produced with the GLAD technique can directly impact various physical properties. The ability to reliably fabricate oriented structures with varying degrees of structural anisotropy allows GLAD to produce films for a variety of different applications.
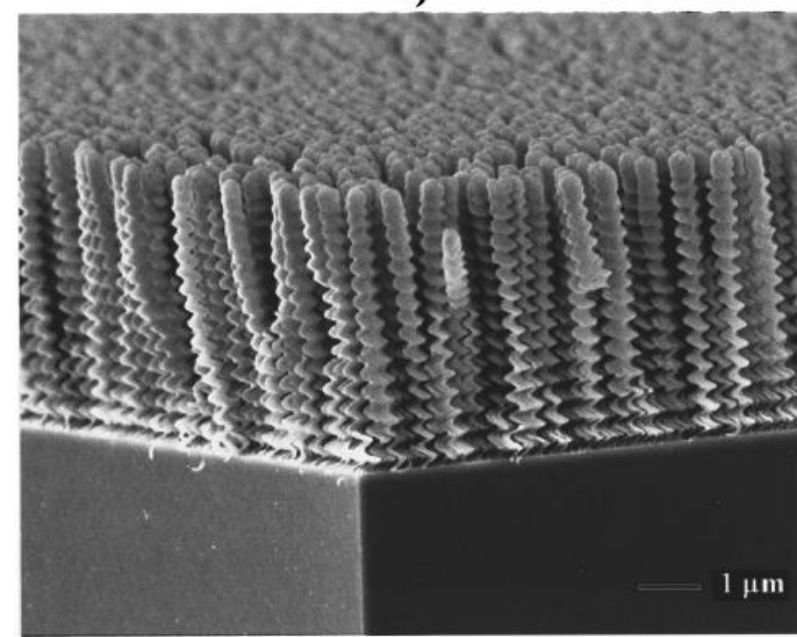
A. Surface area enhancement and applications

B. Mechanical properties

C. Magnetic anisotropy

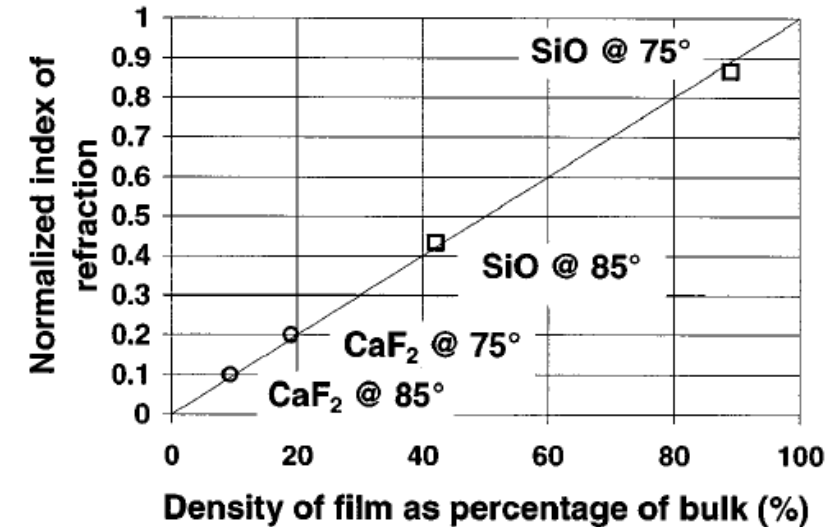## D. Optical properties of structured films

FIG. 7. Normalized effective refractive index as a function of film density. The solid line is a theoretical curve calculated by the density weighted sum of the index of the bulk material and the index of air.